AD 643237

COLLISIONS OF LIQUID DROPS WITH LIQUIDS

PART III. IMPACT CRATERING IN THE HYPERVELOCITY RANGE

OLIVE G. ENGEL

NATIONAL BUREAU OF STANDARDS

Distribution of this
document is unlimited

DEC 12 1966

AIR FORCE MATERIALS LABORATORY
RESEARCH AND TECHNOLOGY DIVISION
AIR FORCE SYSTEMS COMMAND
WRIGHT-PATTERSON AIR FORCE BASE, OHIO

NOTICES

BLANK PAGE

COLLISIONS OF LIQUID DROPS WITH LIQUIDS

PART III. IMPACT CRATERING IN THE HYPERVELOCITY RANGE

OLIVE G. ENGEL

NATIONAL BUREAU OF STANDARDS

Distribution of this
document is unlimited

FOREWORD

This report was prepared by the National Bureau of Standards, Washington, D.C. on Air Force Contract AF 33(657)-62-385, under Task No. 734202, "Studies on the Structure-Property Relationships of Polymeric Materials," of Project No. 7342, "Fundamental Research on Macromolecular Materials and Lubrication Phenomena." The contract efforts were accomplished under the cognizance of the Air Force Materials Laboratory, Research and Technology Division, with the technical work directed by F. W. Kuhn as project engineer.
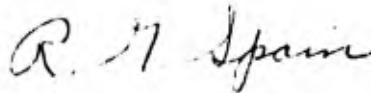
The hypervelocity firings discussed in this report were made at Eglin Air Force Base, where Lt. Thomas E. Shelton was the test officer, and at Arnold Engineering Development Center where Mr. E. H. Goodman and Mr. C. D. Liles of ARO-Inc. were the project engineers.

The work of measuring the apparent crater depths at the National Bureau of Standards and the work of mounting and polishing the crater cross sections and measuring the depth of the projectile residues was done by Mr. Raymond L. Hebert and Mr. David P. David.

Helpful conversation with Dr. George Irwin of Naval Research Laboratory, Washington, D.C., and with Mr. Henry E. Robinson, Chief, NBS Heat Transfer Section are gratefully acknowledged.

Manuscript of this report was released by the author July 1963 for publication as a WADD Technical Report.

This technical report has been reviewed and is approved.

R. G. SPAIN, Acting Chief
Plastics & Composites Branch
Nonmetallic Materials Division
Air Force Materials Laboratory

ABSTRACT

Results of analysis of information obtained from photographs of a hypervelocity impact against a transparent target and from hypervelocity craters produced in impacts that involved the four possible projectile-target combinations of high-purity copper and aluminum are discussed. An equation for hypervelocity crater depth is derived. Hypervelocity crater depth data for the four possible projectile-target combinations of high-purity copper and aluminum are presented in table form and used in graphs to test the theoretical equations.

TABLE OF CONTENTS

ILLUSTRATIONS

TABLES

BLANK PAGE

1. Introduction

Impact cratering has many important applications in the area of erosion. It operates in the erosion of objects that fly at high speed through rain and in the erosion of turbine blades that collide with waterdrops present in wet steam. It is expected to be a problem in the erosion of turbine blades operating with liquid potassium in space vehicles and in the erosion due to the impact of micrometeorites.

Because impact cratering has been the cause of extensive damage already, much work has been done in an effort to understand it and certain facts are known. Craters are formed as a result of impact with liquid drops as well as with solid masses. Furthermore, the mechanism by which crater formation is accomplished appears to vary not only with the material properties of the projectile drop or solid mass and of the target but also with the velocity at which the impact blow is delivered.

1.1 Cratering Mechanisms

When liquid drops and ductile metal spheres impact metal plates at relatively low velocities, the cylinder of metal that extends through the target plate under the area of impact is set in motion as the pressure pulse, initiated by the impact, passes through the plate. Shear stresses, shown schematically as τ_A in Figure 1, exist around this cylinder of metal. Although shear stresses τ_B of Figure 1 also exist in the target metal around the point of impact, the τ_A-shear stresses seem to be the principal cause of impact crater formation in metal plates when the impact velocity is relatively low.

For this mechanism of crater formation the crater depth, D, has been found [1] [a] to be given by

$$D = \left\{ 7.2\, d\, z_p / c_p\, (z_p + z_t) \right\} \left[V - V_i \right] \tag{1}$$

where d is the drop or sphere diameter, c is sound speed, z is acoustic impedance (product of longitudinal wave speed and density) V is impact velocity, and V_i is the lowest velocity at which a crater of noticeable depth is formed. The sub-p notation refers the quantity to the projectile drop or sphere and the sub-t notation refers the quantity to the target. The intercept velocity, V_i, is $19\, E_t\, (z_p + z_t)\, (\rho_p\, c_t\, z_t^3)\, 1/2$ where ρ is density and E_t is the energy per unit volume that can be absorbed by the target metal without fracture or plastic yield. A similar equation, but with different numerical coefficients, has been found to apply for craters produced by the impact of rigid steel spheres [2].

[a] Numbers in brackets refer to literature references at the end of this report.

1
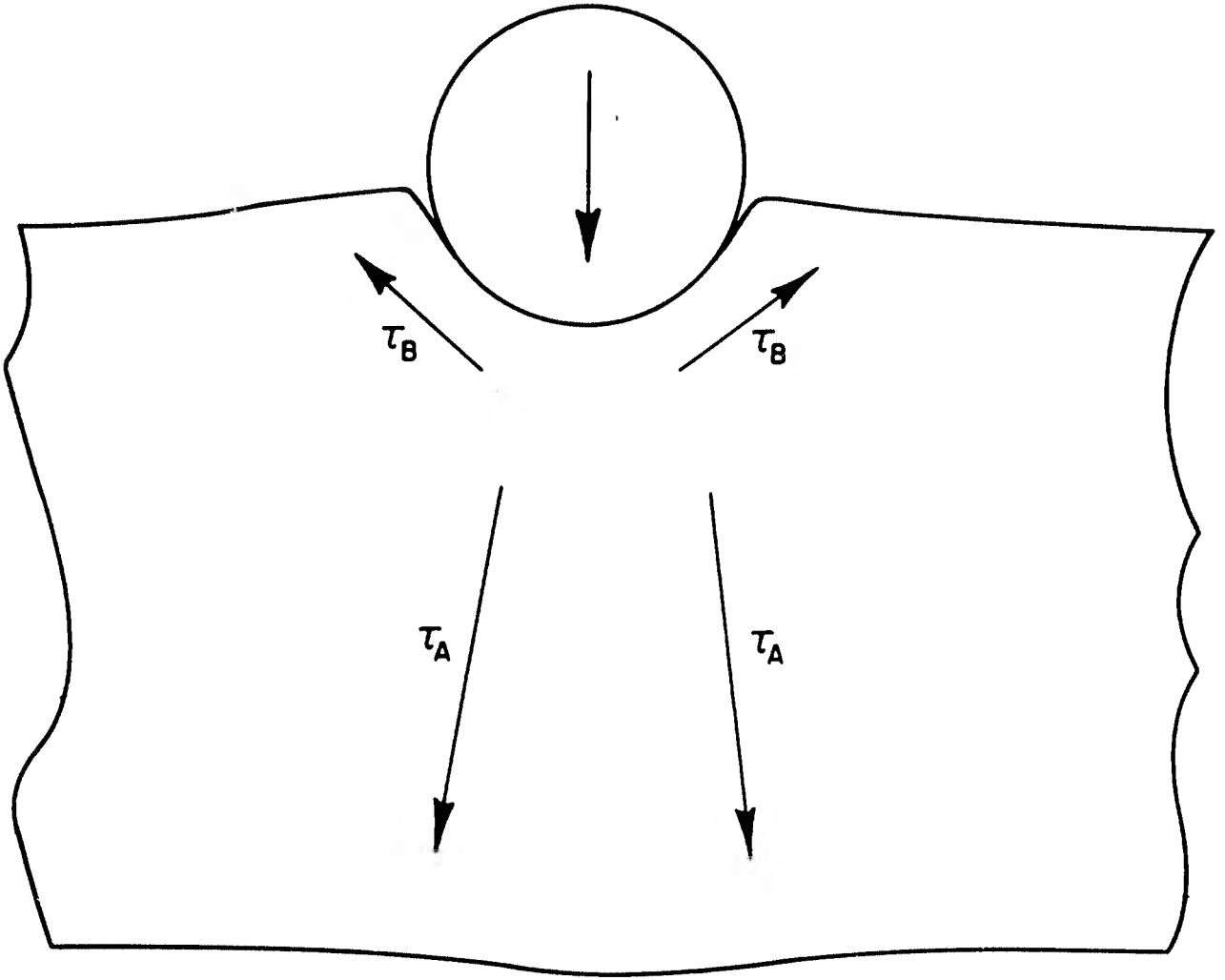
FIGURE 1.   SHEAR STRESSES PRODUCED IN A PLATE BY
AN IMPINGING SPHERE

Impact craters are also formed when liquid drops impinge against target liquids. A detailed study of the behavior of the drop liquid and target liquid when a liquid drop impacts the surface of a body of liquid has been carried out at the National Bureau of Standards [3] . Briefly, the impinging drop delivers a substantial fraction of its energy to the target liquid at the point of impact. A crater forms in the target liquid at this point as a result of the τ_B- shear stresses and a cylindrical wave of target liquid rises around the periphery of the crater. The drop itself flows out radially as it rides down into the target liquid on the receding crater floor.

Stages in the impact of a waterdrop against water are shown in Figure 2. The streamlines in the flow around the enlarging cavity in the target liquid resemble the lines of force around one end of a bar magnet [3] . At the time of maximum cavity depth, motion along the streamlines stops. After the time of maximum cavity depth, motion is resumed; it is, however, reversed in direction. See Figure 3.

The quantitative study of liquid-drop-versus-liquid impacts that has been carried out so far [3] has covered only the case that the drop and target liquids are the same. For this case the impinging drop gives about half of its energy to the target liquid and the crater formed in the target liquid is essentially hemispherical at its time of maximum depth (see Figure 2). For the essentially hemispherical craters, which are produced when the drop and target liquid are the same, it has been found [3] that the maximum crater depth, D, is given by

$$D = \left[(\left\{ d^3 V^2 / 6.6667\ g \right\} + \left\{ 311.49\ \gamma^2 / g^2\ p^2 \right\})^{1/2} - 17.649\ \gamma / g \right]^{1/2} \quad (2)$$

where γ is the surface tension of the liquid used for drop and target and g is the acceleration due to gravity. From pictures taken by Rupe [4] , it appears that if the drop is of a higher density liquid than the target the crater will resemble a hemi-prolate spheroid.

Fror eq. (1), the maximum depth of craters formed in metal plates by impact of liquid drops or ductile metal spheres varies as V^1. From eq. (2) the maximum depth of craters formed in target liquids by impact of a liquid drop varies as $V^{1/2}$. Crater depth in hypervelocity impacts has been found to vary as $V^{2/3}$ over a wide velocity range the upper limit of which has not yet been determined with certainty [5] . It is noteworthy that $V^{1/2} < V^{2/3} < V^1$ and that on the basis of the variations of crater depth with impact velocity the hypervelocity cratering mechanism that operates in the velocity range for which the $V^{2/3}$-power law applies may be intermediate between that for which the target is a solid and that for which the target is a liquid.
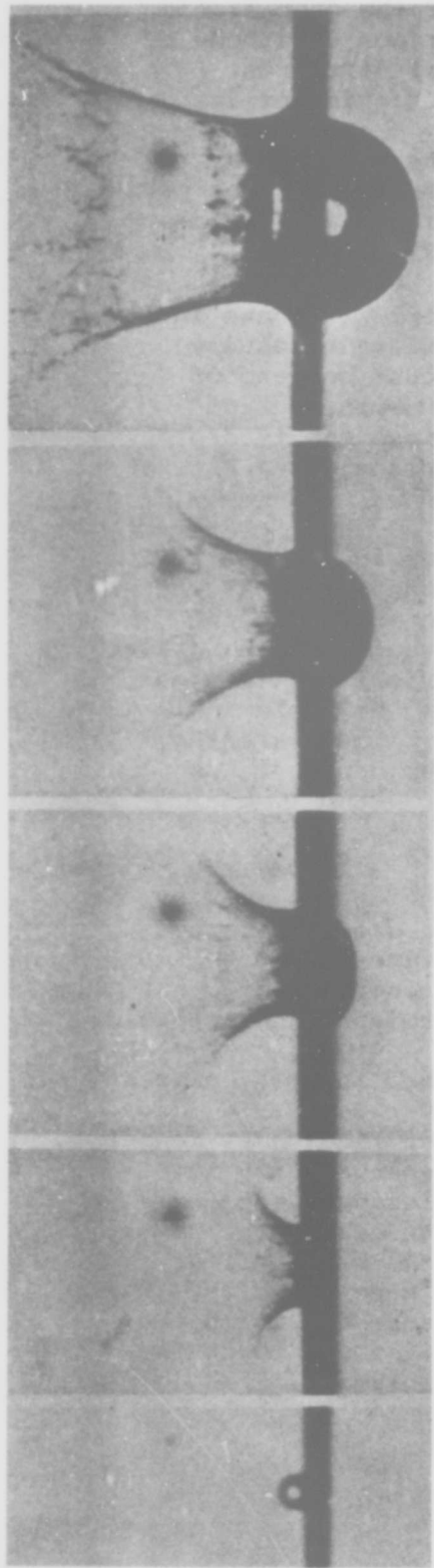
AT IMPACT   AFTER 0.33 m sec   AFTER 0.65 m sec   AFTER 0.98 m sec   AFTER 2.9 m sec
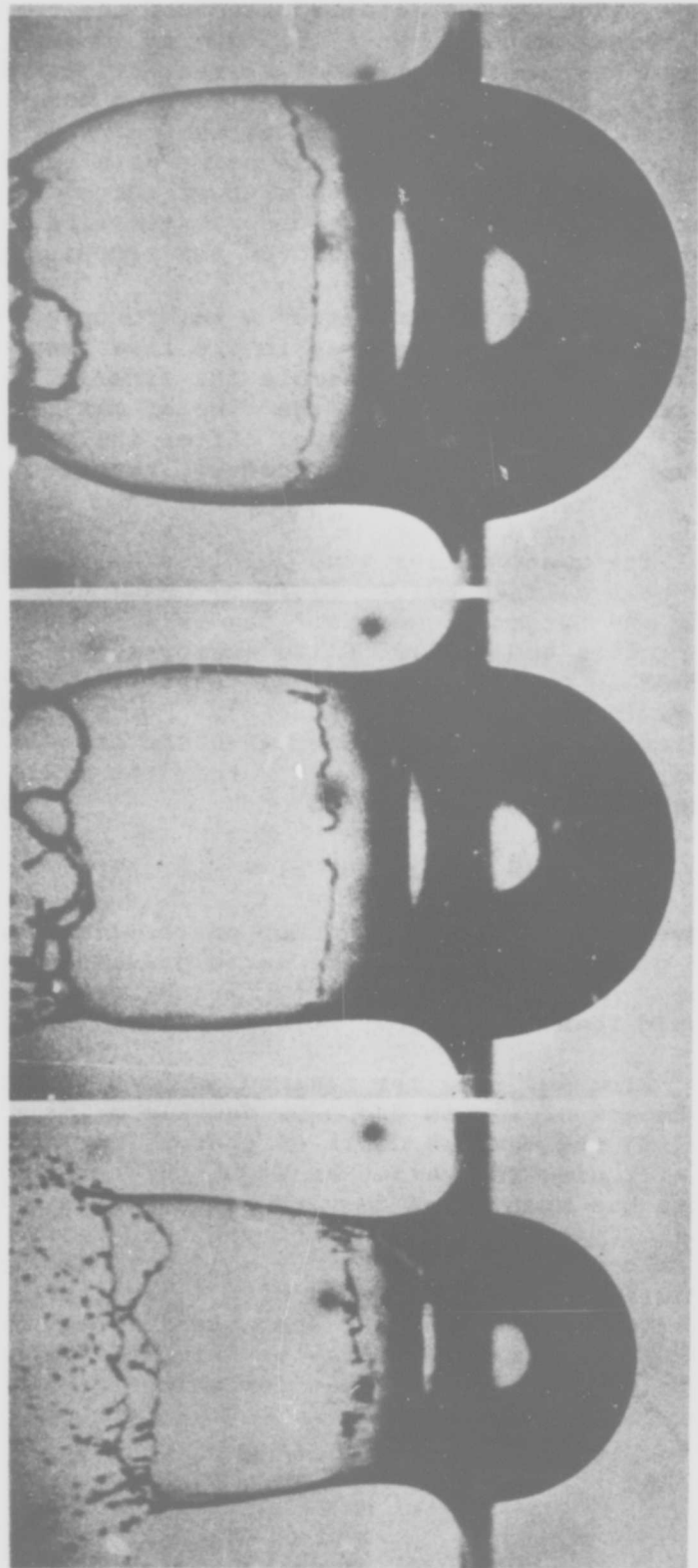
AFTER 8.2 m sec   AFTER 16.4 m sec   AFTER 27.5 m sec

FIGURE 2.   IMPACT OF A WATERDROP AGAINST WATER
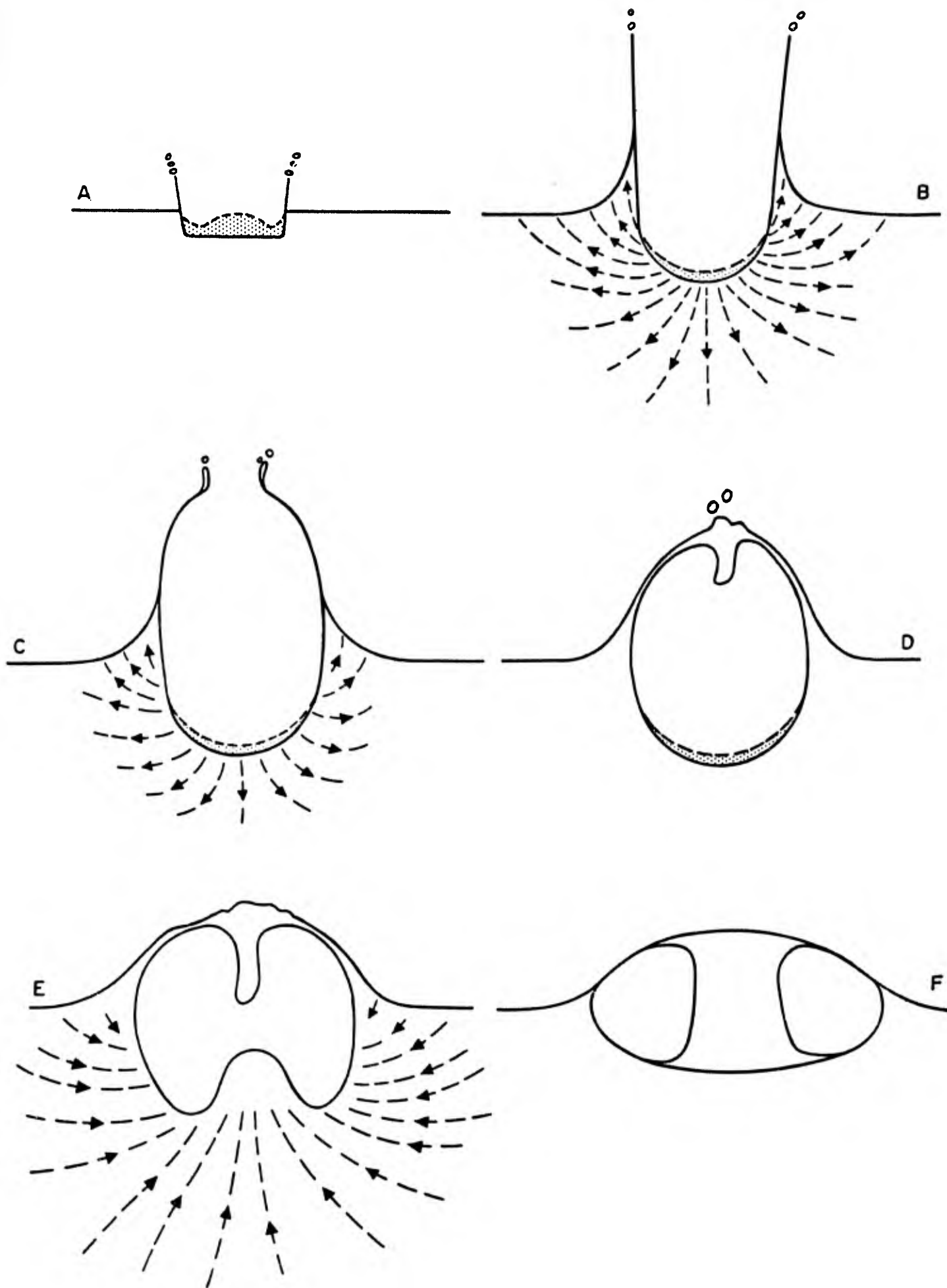
FIGURE 3.   STREAMLINES IN THE FLOW AROUND AN IMPACT
CRATER IN WATER

The regions in which these power laws apply as impact velocity is increased are shown schematically in Figure 4. The V^1-power law applies to impact against a solid target plate where the τ_A-shear stresses are the principal cause of crater formation. The $V^{1/2}$-power law applies to impact against a fluid target where the τ_B-shear stresses govern crater formation; the fluid target may be a real liquid or a solid that has been raised to a state of such high energy density that it flows like a liquid. The $V^{2/3}$-power law seems to apply to impacts in which the target displays a quasi-fluidity but in which the τ_B-shear stresses cause the crater formation. Between these regions there must be transition regions in which more than one cratering mechanism contributes; this is indicated by stippled bands in Figure 4.

1.2 Impact Mechanics

When a solid sphere impacts a planar solid target at normal incidence, two pressure waves are initiated at the impact surface as is shown schematically in Figure 5. Pressure wave A of Figure 5 moves into the target; pressure wave B of Figure 5 moves into the sphere. For hypervelocity impacts these pressure waves are shock waves. The particles of solid in both sphere and target that have been traversed by these shock waves have been given energy. The pressure, density, temperature, and entropy of the solid matter traversed by these shock waves have been increased. For impacts at very high velocity the compressed target metal that has been traversed by shock wave A of Figure 5 in the initial phase of the impact has such high energy density that it must flow as a result of the τ_B-shear stress of Figure 1; the compressed metal in the sphere must also flow.

When shock wave B of Figure 5 reaches the bounding surface of the sphere, it reflects as a tension wave that moves back toward the impact surface. As this reflected tension wave traverses the sphere, the heated metal of the sphere, which is in a state of high energy density and is undergoing a fluid-like flow, is released from compression. Fusion of this metal is to be expected if its temperature after pressure release is in excess of the melting point that is characteristic of the increased entropy state in which it exists.

When the reflected tension wave reaches the surface of contact between the impacted sphere and the target, it is partly transmitted into the target and partly reflected back into the sphere. The heated target metal, into which the tension wave is partly transmitted, which is in a state of high energy density, and which is undergoing a fluid-like flow as a result of the τ_B-shear stresses, will now also undergo fusion if its temperature after pressure release is in excess of the melting point that is characteristic of the increased entropy state in which it exists.

6
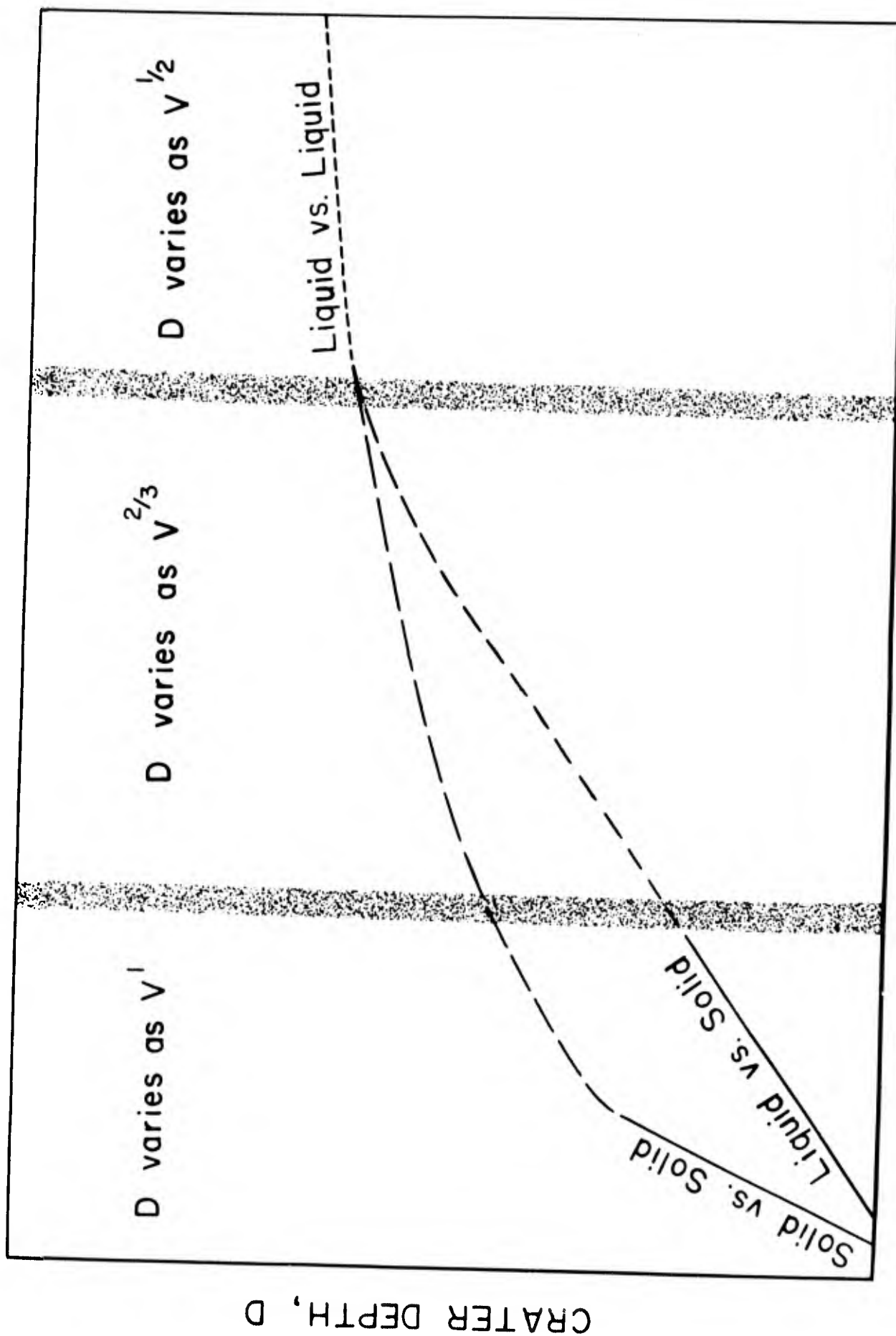
FIGURE 4. SCHEMATIC REPRESENTATION OF CRATERING REGIMES

7
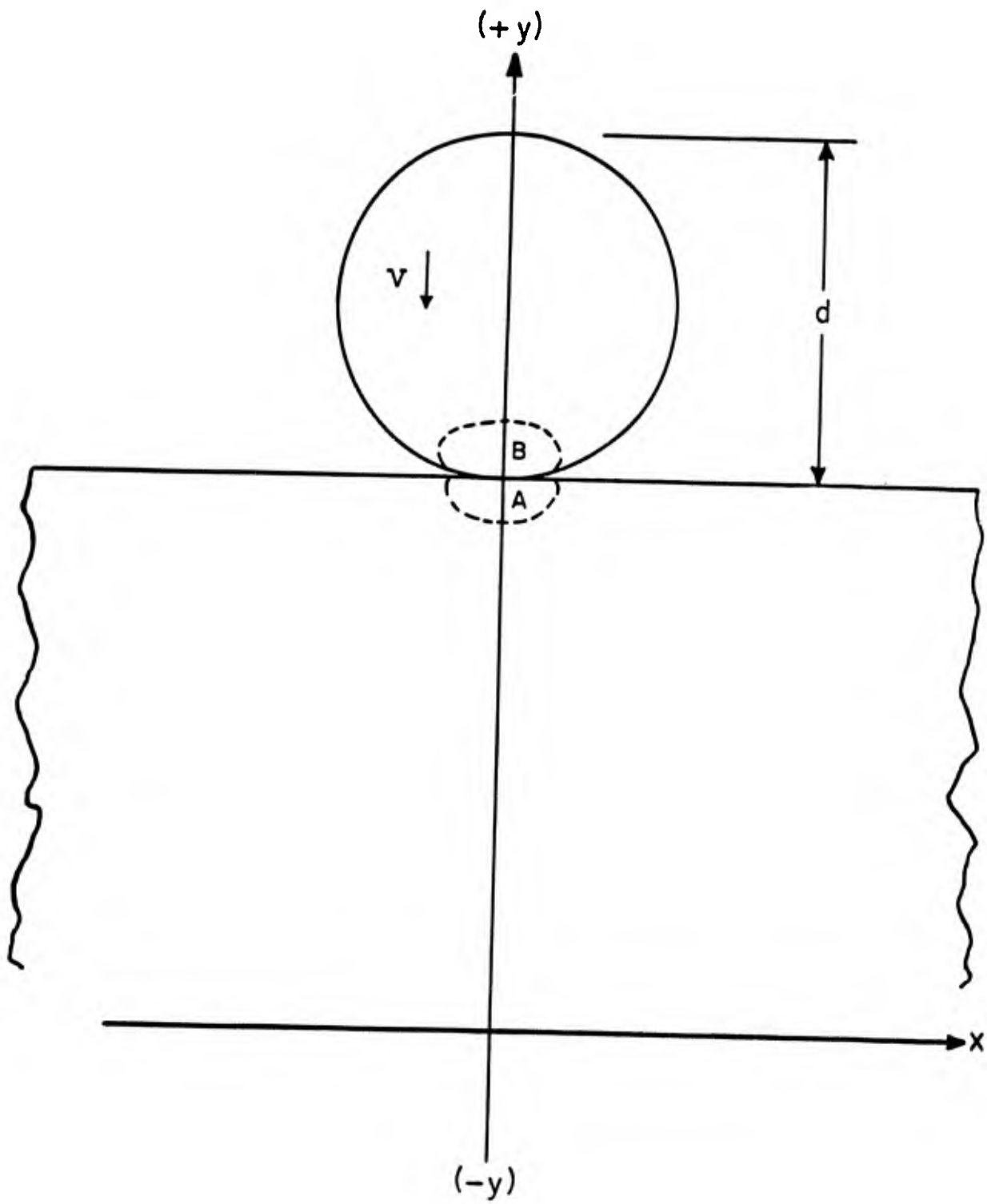
FIGURE 5.   SCHEMATIC REPRESENTATION OF A SPHERE IMPACTING A PLATE

8

As the impact velocity is progressively increased, the amplitude of the transmitted wave of tension will increase and the amount of target metal that melts will increase. If the impact velocity is progressively increased, a velocity range should be encountered in which fusion of target metal accompanied by the outward flow of the melt as a result of the τ_B-shear stresses should become the dominant process in determining crater size. By means of a theoretical treatment, Olshaker and Bjork [6] have found that the threshold velocities for incipient melting in impacts involving three of the four possible projectile-target combinations of copper and aluminum are: copper-copper, 4.4 km/sec; aluminum-aluminum, 5.0 km/sec; and aluminum-copper, 6.6 km/sec.

At somewhat lower velocities the same cratering mechanism will operate because of the quasi-fluid flow of target material that is in a state of very high energy density. In metal plates, at still lower velocities, there is probably a transition region in which the low-velocity cratering mechanism [1,2] governed by the τ_A-shear stresses of Figure 1 contributes in determining the crater size.

2. Analysis of Some Aspects of Hypervelocity Cratering

The first analysis of any problem in phenomenological. Various aspects of hypervelocity cratering have already been reported and discussed [7].

An experiment was designed at the National Bureau of Standards to collect a variety of quantitative hypervelocity cratering data that would provide a stringent test of a theoretical crater depth equation [b]. The first phase of the experiment called for the collection of cratering data for impacts of the four possible projectile-target combinations of high purity copper and aluminum. A later phase of the experiment called for impacts made with use of plastic materials. Although the investigation was terminated after completion of only the first phase, two shots were fired with use of plastic projectiles and transparent plastic targets.

Inspection of the targets after the firings were accomplished and of Beckman and Whitley framing camera pictures of the impacts provided valuable information with regard to the crater-forming process.

2.1 Information from Impact Against a Transparent Target

Stages in the impact of a 7.62-mm (0.3-in.) right circular cylinder of polycarbonate resin against a 4.9-cm (1.9-in.)-thick plate of poly(methyl methacrylate) at a velocity of 663,490 cm/sec (21,768 ft/sec) are shown in Figure 6. In section 1 of Figure 6,

---

[b] The details of data collection for this experiment and the source of the hypervelocity firings are given in section 4.

distinct separation of the outward-moving hemispherical pressure
wave produced by the impact, which was indicated schematically as
pressure wave A in Figure 5, can be seen after an elapsed time of
$2.2\,\mu$ sec. At this time the outline of the pressure wave is a band
rather than a line. Measurements of the radius of the hemispherical
pressure wave were made [c]/ up to an elapsed time of $9.2\,\mu$ sec; they
are listed in Table I. The slope of the plot of these radii against
elapsed time indicates that the group velocity of the pressure wave
is far in excess of the speed of sound in the target material. At
an elapsed time of less than 1   sec its velocity is of the order
of the speed of sound in the target material plus one half of the
impact velocity.

From inspection of Figure 6, the target material that has
been traversed by the shock wave of pressure remains transparent.
It is not noticeably different from the as-yet undisturbed material
of the remainder of the plate. However, where one of the 1-inch
grid lines, which were photographed with the impact for measurement
purposes, is viewed through it (see Figure 6, section 2), the grid
line is seen to be distorted. If a line is viewed through an empty
round-bottom flask it is not distorted, but if the round-bottom
flask is filled with water a line viewed through it undergoes the
same kind of distortion as that suffered by the grid line. From
this it may be deduced that the distortion of the grid line is not
produced by the hemispherical shell of the shock front but rather
by a change in specific refractivity of all of the material that
has been traversed by the shock front. This material is under high
pressure and is in a higher density state than the undisturbed
material of the remainder of the target plate.

---

[c]/ The measured distances were obtained in terms of the distance
between the 1-inch grid lines. They are not corrected for the fact
that the grid was located a short distance behind the impinging
projectile.

TABLE I

Measurements on the Views of Figure 6, Sections 1 and 2

Elapsed Time t	Cavity Depth D	Neck of Ejecta N	Ratio of D/N	Shock Wave Radius
sec	cm	cm	-	cm
2.2	0.77	1.31	0.59	1.29
3.1	0.84	1.44	0.58	1.58
3.9	1.04	1.57	0.66	1.92
4.8	1.13	1.67	0.68	2.20
5.7	1.24	1.83	0.68	2.51
6.6	1.30	1.91	0.68	2.80
7.4	1.38	2.05	0.67	3.08
8.3	1.41	2.14	0.66	3.38
9.2	1.40	2.26	0.62	3.63

BEFORE IMPACT

AFTER 0.42 μ sec

AFTER 1.3 μ sec

AFTER 2.2 μ sec

AFTER 3.1 μ sec

AFTER 3.9 μ sec

AFTER 4.8 μ sec

AFTER 5.7 μ sec

AFTER 6.6 μ sec

AFTER 7.4 μ sec

FIGURE 6, SECTION 1. HYPERVELOCITY IMPACT OF A POLYCARBONATE RESIN CYLINDER
AGAINST A POLY(METHYL METHACRYLATE) PLATE

AFTER 10.1 μ sec

AFTER 12.7 μ sec

AFTER 9.2 μ sec

AFTER 11.8 μ sec

AFTER 8.3 μ sec

AFTER 11.0 μ sec

FIGURE 6, SECTION 2. HYPERVELOCITY IMPACT OF A POLYCARBONATE RESIN CYLINDER
AGAINST A POLY(METHYL METHACRYLATE) PLATE

13

At an elapsed time of 16.2 μ sec (see Figure 6, section 3), the shock wave of pressure has reached the opposite face of the target plate and has reflected as a tension wave because this face of the target was maintained as a free surface. A dark area is seen to be formed in the leading part of the reflected tension wave. There is a gap between this dark area and the line of darkening on the reverse face of the plate where the pressure wave reflected as a tension wave. It is reasonable to suppose that this gap is the region of superposition of the reflected tension wave and the original pressure wave. In terms of this interpretation, darkening occurs in target material that is subjected to a high tensile stress (the darkening is due to crazing or fracture that results in light interference) and the net tension in the region of superposition is too low to produce darkening.

From Figure 6, section 4, it can be seen that after an elapsed time of 19.7 μ sec the grid line at the center of the target plate is no longer noticeably distorted. When, however, the tension wave, which reflected from the rear face of the plate and is now moving toward the impact face, has passed over it (see Figure 6, section 5), it is bowed in the opposite direction to that observed in the views of Figure 6, section 2. The target material traversed by the tension wave is in a state of tension; its density has been reduced. In the views of Figure 6, section 5, the leading surface of the tension wave is no longer accompanied by darkening. This suggests that the material that is being traversed by the reflected tension wave at this time is being subjected to a tensile stress of reduced intensity.

The two features of greatest interest in the views of Figure 6 are the black hemisphere from which the shock wave of pressure detaches at an elapsed time of 2.2 μ sec and the black structure which moves down from the surface and eventually obscures the black hemisphere at an elapsed time of 10.1 μ sec. Specific attributes of these structures are considered below.

The depth of the black hemisphere below the surface of the target was measured in the various pictures of Figure 6 in which the bottom of the hemisphere can be seen before it is completely obscured; they are listed in Table I. The measured values of depth are plotted against elapsed time in Figure 7 using two time scales. They are plotted as open circles using the 10-μ sec time scale and as solid circles using the 100-μ sec time scale. From the locus of the open circles it can be seen that the black hemisphere reached maximum depth at an elapsed time of 8.3 μ sec.

The depth of the cavity that was produced in water by impact of a waterdrop is also plotted against elapsed time in Figure 7. The points are indicated with triangles and the 40 m sec time scale

14

AFTER 13.6 μ sec

AFTER 14.5 μ sec

AFTER 15.3 μ sec
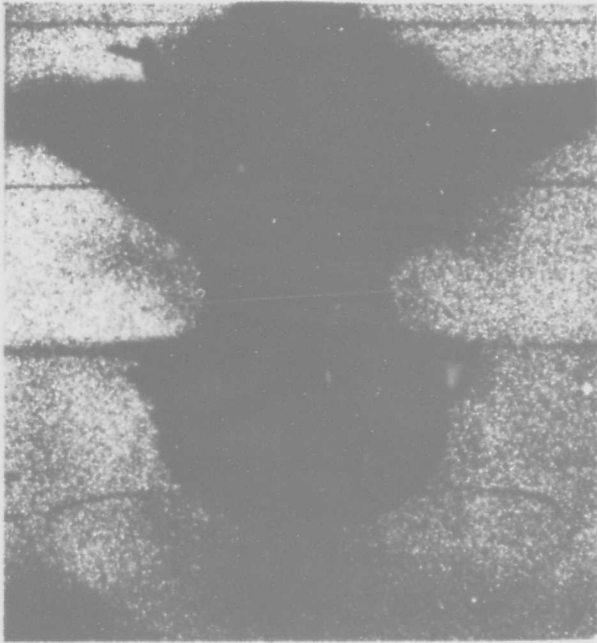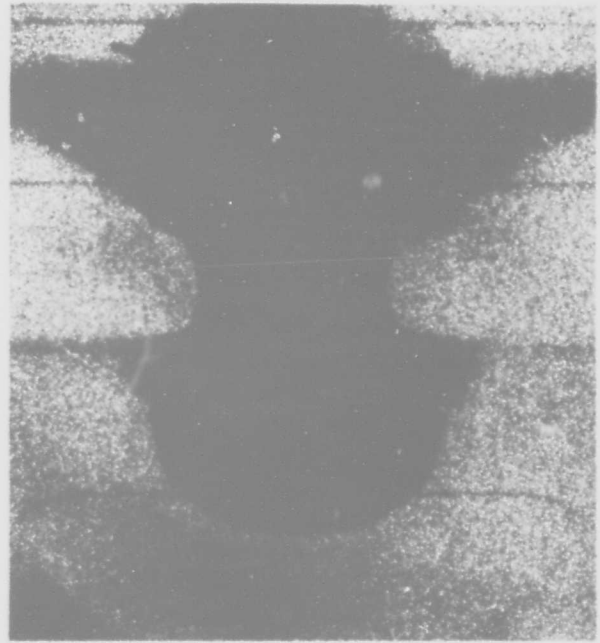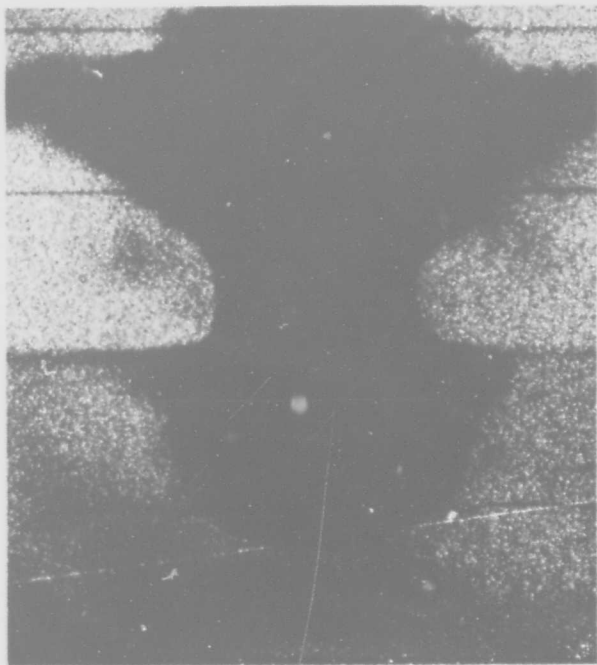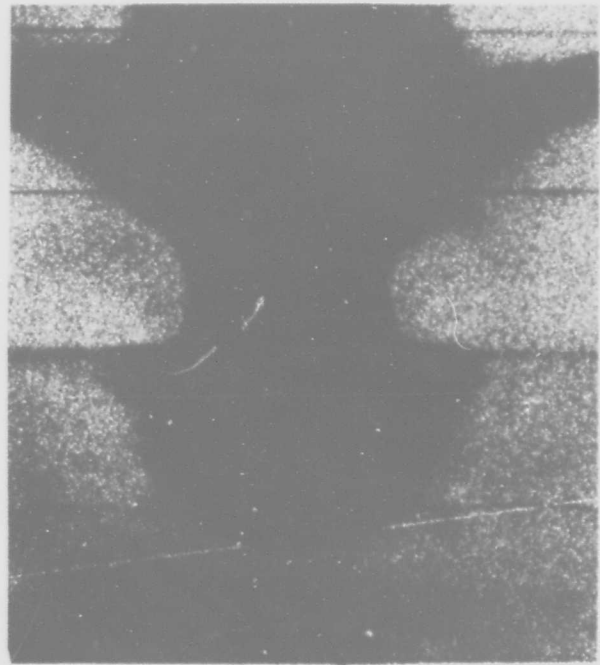
AFTER 16.2 μ sec

FIGURE 6, SECTION 3. HYPERVELOCITY IMPACT OF A POLYCARBONATE RESIN
CYLINDER AGAINST A POLY(METHYL METHACRYLATE) PLATE

AFTER 17.1 μ sec   AFTER 18.0 μ sec
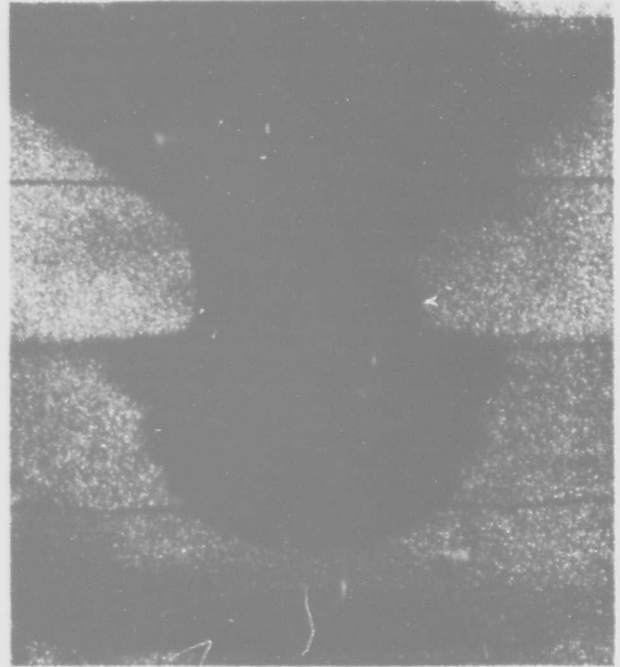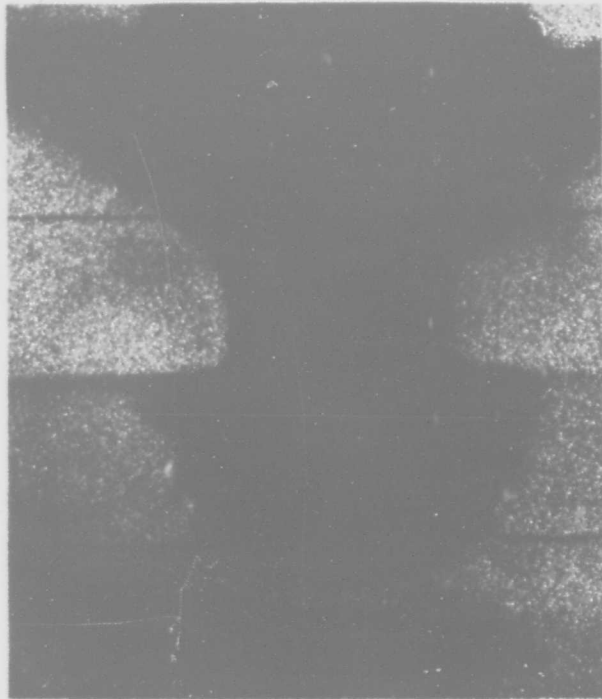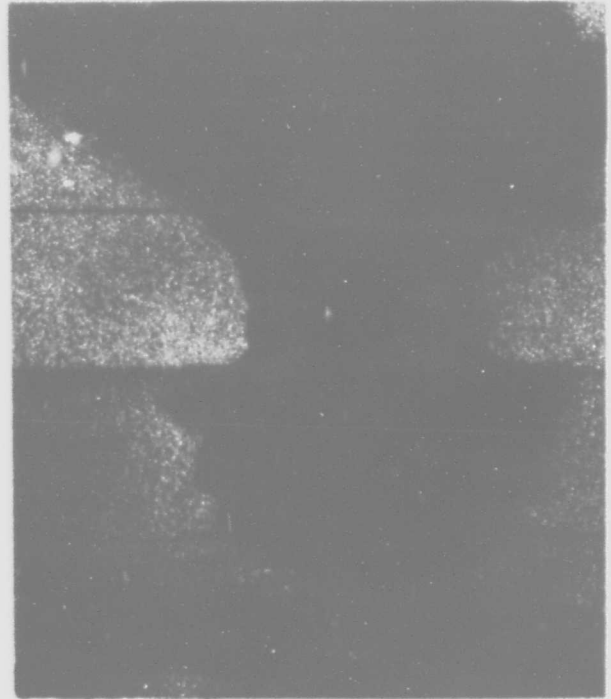
AFTER 18.9 μ sec   AFTER 19.7 μ sec

FIGURE 6, SECTION 4.   HYPERVELOCITY IMPACT OF A POLYCARBONATE RESIN
CYLINDER AGAINST A POLY(METHYL METHACRYLATE) PLATE

16

AFTER 31.1 μ sec
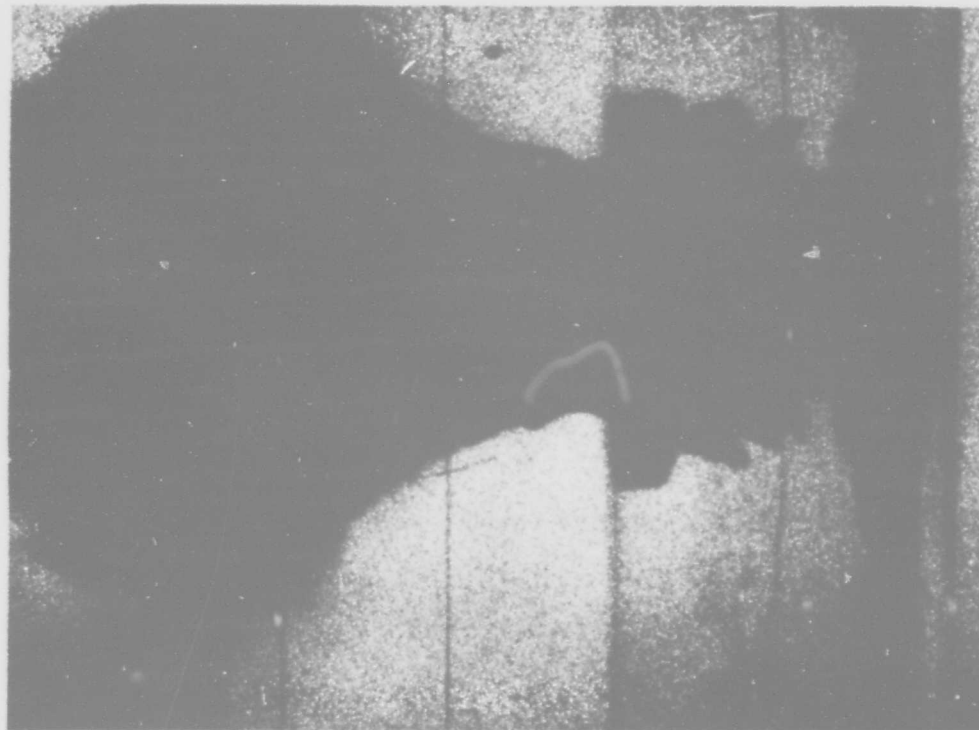
AFTER 22.4 μ sec

FIGURE 6, SECTION 5. HYPERVELOCITY IMPACT OF A POLYCARBONATE RESIN CYLINDER
AGAINST A POLY(METHYL METHACRYLATE) PLATE

17
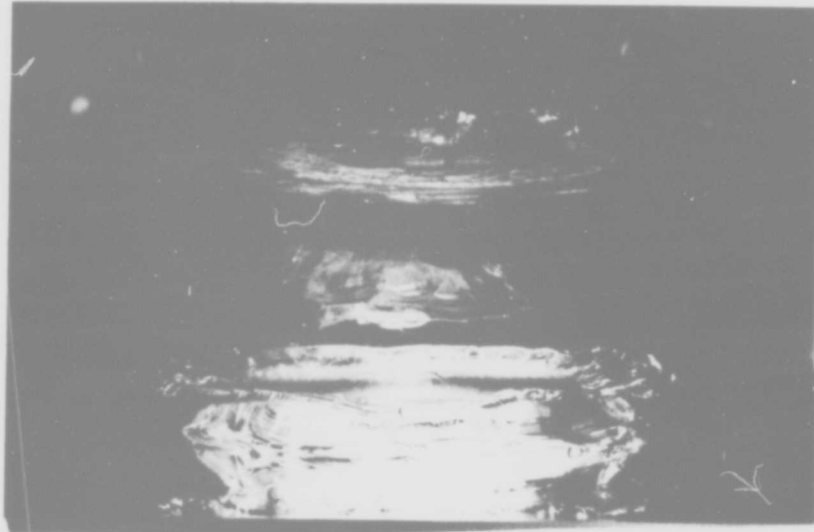
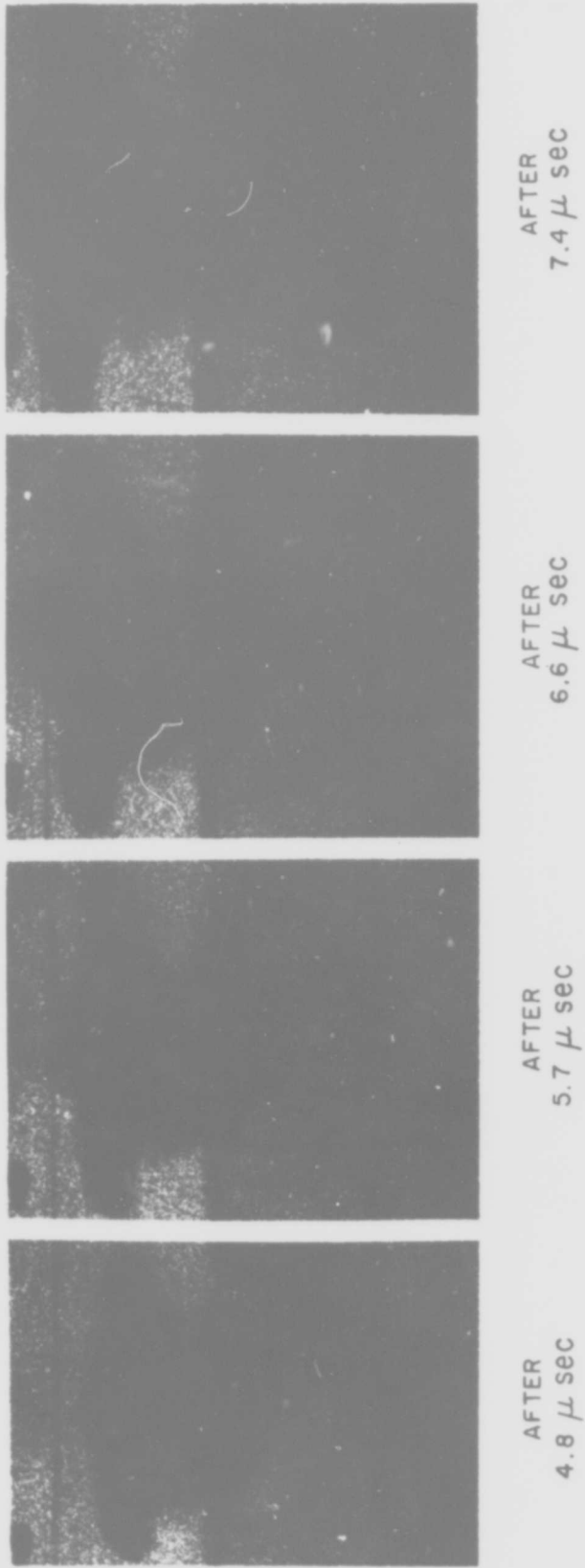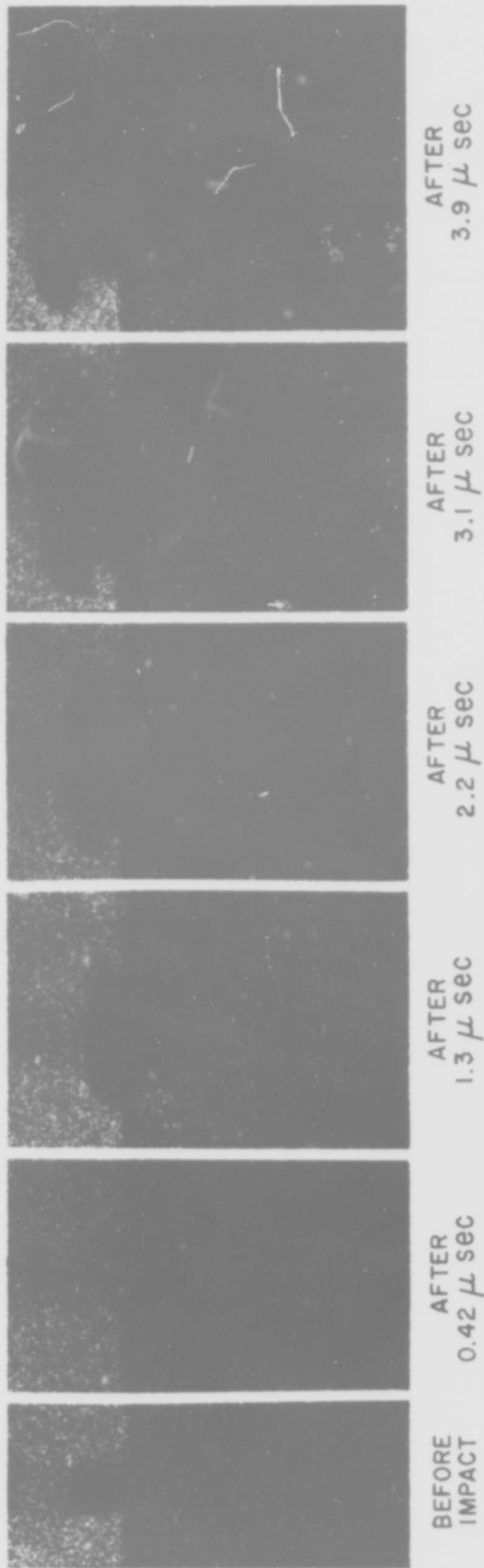A. TOP VIEW OF DAMAGE
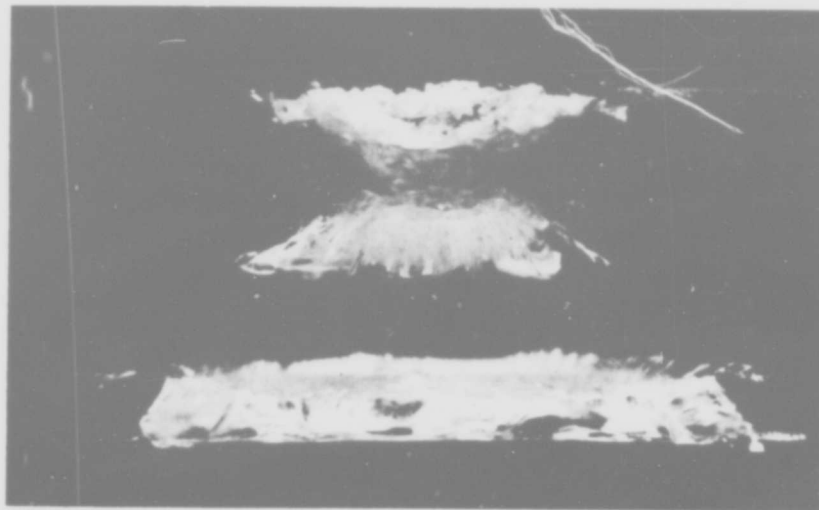
B. CROSS - SECTIONAL VIEW
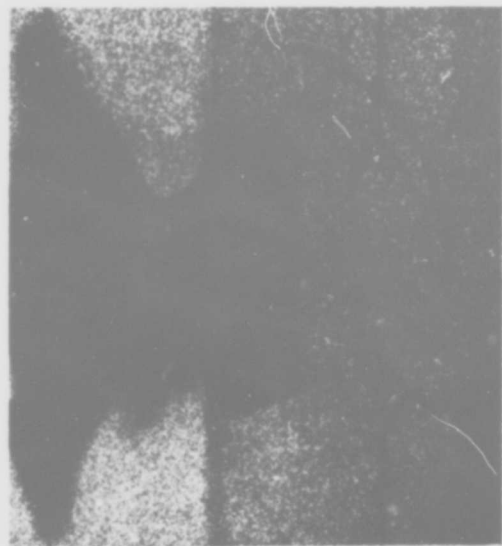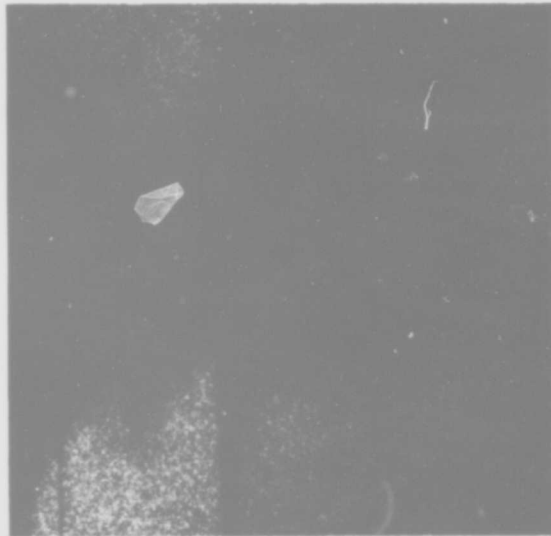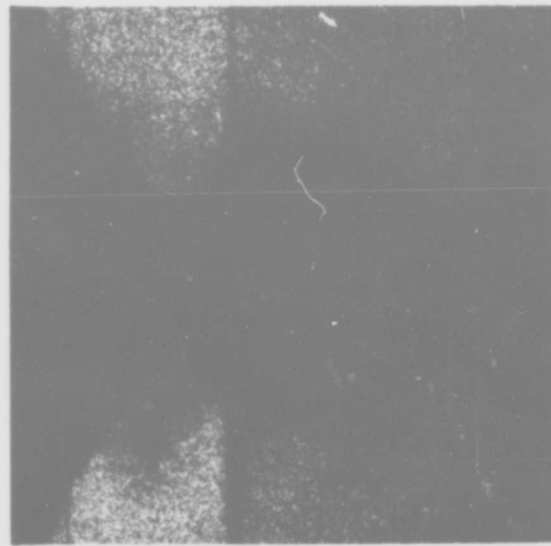
FIGURE 6, SECTION 6. HYPERVELOCITY IMPACT OF A
POLYCARBONATE RESIN CYLINDER AGAINST A
POLY(METHYL METHACRYLATE) PLATE

18
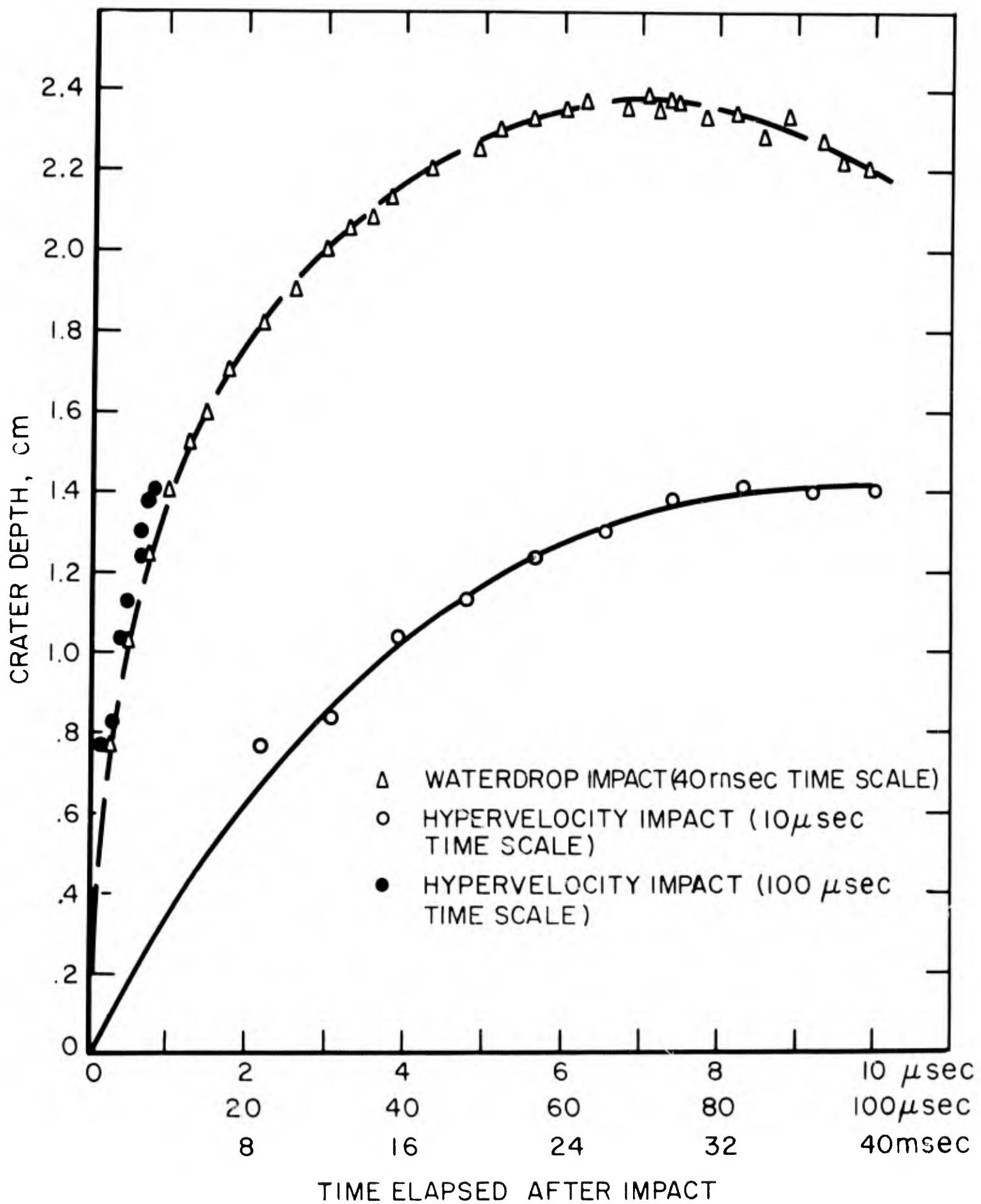
FIGURE 7. TIME DEPENDENCE OF CRATER DEPTH

19

is used. Comparison of the locus of the solid circles with that of the triangles suggests that, although the black hemisphere reached its maximum size in 1/3500 the time that was required for the cavity produced in water by impact of a waterdrop to reach maximum size, it may have been following a somewhat similar law of growth.

An important difference between the black hemisphere shown in Figure 6, sections 1 and 2, and the cavity produced in water by impact of a waterdrop shown in Figure 2 is that the black hemisphere has no high light; the light interference that it produces is similar to what would be produced by an opaque object.

Physical evidence indicates that the polymeric target material traversed by the high amplitude shock wave of pressure should remain solid. Poly(methyl methacrylate) goes through a second order transition to the glassy state at a temperature of about $105^{\circ}C$ [8]. Furthermore, the inside walls of the crater as seen in the poly(methyl methacrylate) plate after the impact are darkened, which suggests that not only the glass transition temperature but even the decomposition temperature of the polymer was reached. However, the density of mobile polymeric material above the glass transition temperature is normally less than the density of the rigid material below this temperature. The same state of affairs is found in metals where, in most cases, the density of the fluid state is less than the density of the solid state. Fluidity should, therefore, not be fostered by imposition of high pressure and the target material traversed by the high amplitude shock wave of pressure would be expected to remain in the rigid state.

Whether of not the black hemisphere is an empty crater cannot be determined from the pictures but the evidence just given suggests that its bounding walls are of solid polymeric material. Rigid polymers craze when they are subjected to tension, and crazing would result in light interference that would produce darkening in the photographs as was pointed out above in discussing the tension wave that reflects from the reverse face of the target plate. If it is supposed that the black hemisphere is an empty enlarging crater in solid polymeric material, its walls would be under tension; they would be expected to craze, and to appear dark and without a high light when photographed, as is in agreement with the observations given. That the black hemisphere is an empty enlarging cavity is, therefore, a reasonable supposition.

The funnel-shaped mass of ejecta, which rises above the surface of the target in the pictures of Figure 6, is the counterpart of the cylindrical wave of target liquid in liquid-drop-versus-liquid-target

20

impacts (see Figure 2). If attention is fixed on the neck of this structure in Figure 6 it can be seen that, below the neck, the structure flares outward as it meets the surface of the target just as the true liquid wave does in the views of Figure 2. In the true liquid impact the point at which the curve of the superstructure merges with the target surface is roughly one cavity diameter from the point of impact.

If the black hemisphere is an empty cavity, it must have been formed by a fluid-like flow of target material in a state of extremely high energy density along streamlines similar to those of Figure 3. Inspection of the pictures of Figure 6, section 1, at elapsed times of 1.3 to 3.1 μ sec shows that the outward flare of the ejecta below the neck in this structure merges with the target surface <u>within</u> the confines of the black hemisphere. Consequently, at this time the black hemisphere must be larger than the empty impact crater that it obscures. At an elapsed time of 3.9 to 4.8 μ sec the outward flare below the neck in the structure of the ejecta merges with the surface <u>beyond</u> the confines of the black hemisphere. And at an elapsed time of 5.7 μ sec a dark structure forms immediately under the area over which the outward flare below the neck in the ejecta meets the target surface. This dark structure moves down into the target. It has obscured roughly 2/3 of the black hemisphere at an elapsed time of 8.3 μ sec when the black hemisphere reaches maximum size. The fact that the black hemisphere reaches maximum depth when only 2/3 of it obscured suggests that the dark structure moving down from the surface may not control the size to which the black hemisphere grows; it may, however, be checking free flow of the target material through which it has passed. It obscures the black hemisphere at an elapsed time of 10.1 μ sec.

The target material in the outward flare below the neck in the ejecta was released from compression as it flowed upward around the rim of the cavity. This pressure-released material moved out radially over the transparent solid target beyond the confines of the black hemisphere at an elapsed time of 3.9 to 4.8 μ sec. It is possible that the dark structure that originates under the area covered by this pressure-released material is a wave of tension (relief) having high energy density which results in crazing in the solid target material traversed by it. Light interference by the crazed material would result in darkening in the photographs. The leading surface of the dark structure has the same diameter at an elapsed time of 10.1 μ sec as it had at an elapsed time of 5.7 μ sec, when it originated at the target surface; it is progressively somewhat broader at points closer to the target surface.

21

The appearances that have been described and the inter-
pretations that have been tentatively advanced suggest a two-stage
model for the hypervelocity cratering process. The first stage
may be hydrodynamic flow of compressed target material in the state
of high energy density as has been suggested for the hyrodynamic
model of hypervelocity cratering $\angle 7\overline{J}$. This flow should have
streamlines similar to those in Figure 3, which are determined by
the pressure distribution in the target material around the cavity,
and should result in a crater which is approximately hemispherical
if the projectile and target materials are the same, or, more exactly,
if they have the same acoustic impedance. Crater shape is discussed
in considerable detail below. The second stage envisaged should be
different for different target materials. In the case of ductile
metals, it may be continued fluid flow or quasi-fluid flow. In
the case of brittle materials of relatively low strength, it may
be crazing and fracture of pressure-released target material that
has been traversed by the tension wave that originates at the surface.
Not only the energy density in the pressure-released target material
but also its characteristic mode of failure (ductile flow or brittle
fracture) should determine which of the possible responses will occur.

2.2 Information from Hypervelocity Impacts Against Metal Targets

Crater depth and crater depth/diameter ratio for hypervelocity
impact of 3/16-inch copper spheres against copper plates and for
3/16-inch aluminum spheres against aluminum plates are plotted
against velocity in Figure 8. From the curves of Figure 8 it
can be seen that crater depth for the copper-projectile-copper-
target combination is about 0.1 cm greater than for the aluminum-
projectile-aluminum-target combination in the velocity range for
which data are given. A plot of similar data for 1/8-inch spheres
produced essentially the same result. Also, the depth/diameter
ratio for the copper-projectile-copper-target combination varies
roughly between 0.55 and 0.59 whereas that for the aluminum-pro-
jectile-aluminum-target combination varies between 0.52 and 0.56.
Both of these differences are of the order of 10 per cent.

A plot of the depth/diameter ratio obtained for impacts of
copper spheres against copper targets using spheres of three diff-
erent diameters is shown in Figure 9. Two conclusions can be drawn
from the plot: (1) depth/diameter ratio is not a function of the
size of the impinging sphere, and (2) the trend of depth/diameter
ratio with increasing velocity is toward the limiting value of 0.5.

When the spherical projectile and the target are of different
metals, wide differences in crater size and shape are found for
impacts in which the projectile diameter and impact velocity are
the same. The depth/diameter ratio produced by hypervelocity impact
of 1/8-inch spheres for each of the four possible projectile-target
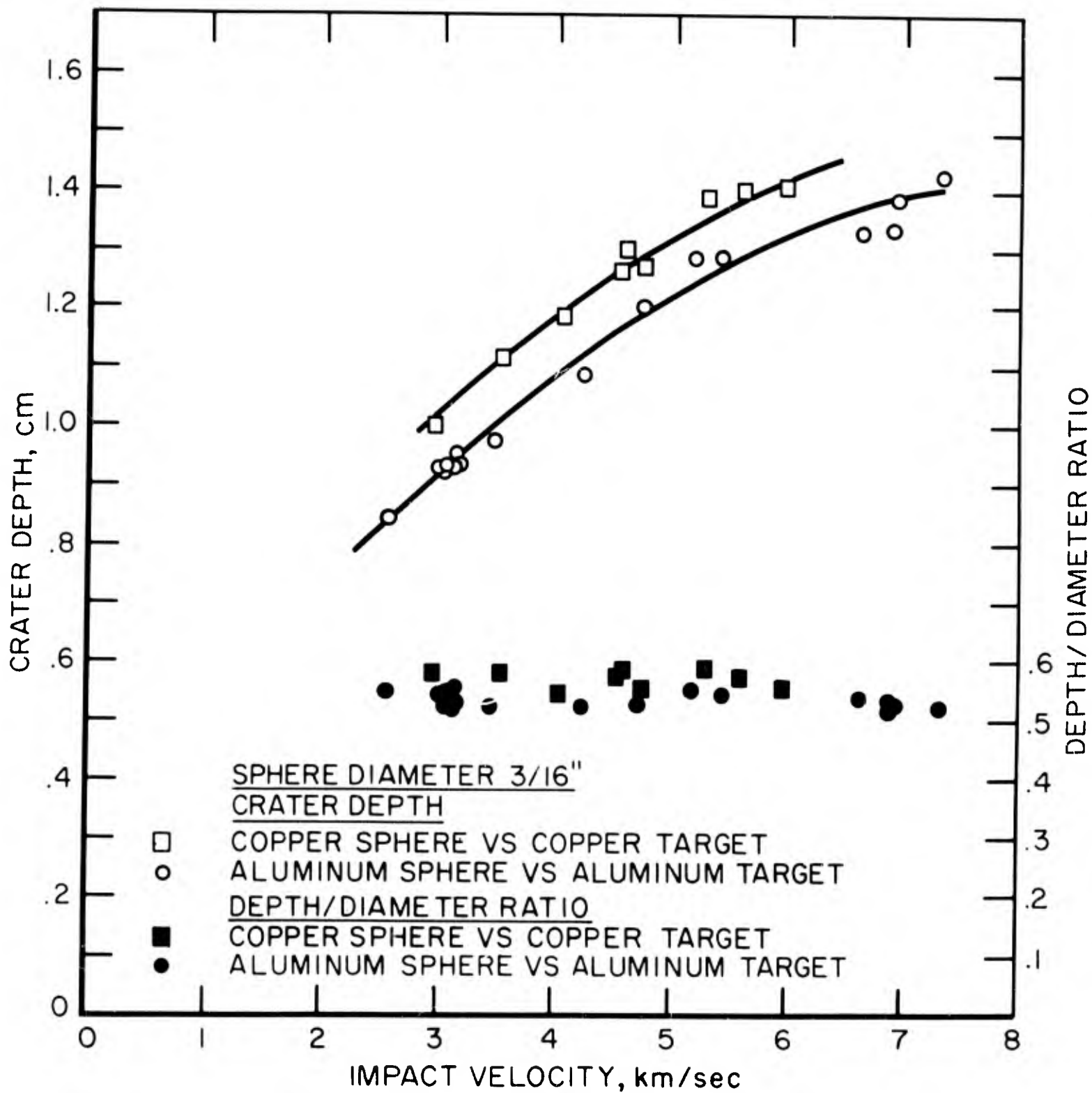
FIGURE 8. CRATER SIZE FOR SIMILAR PROJECTILE-TARGET COMBINATIONS

23
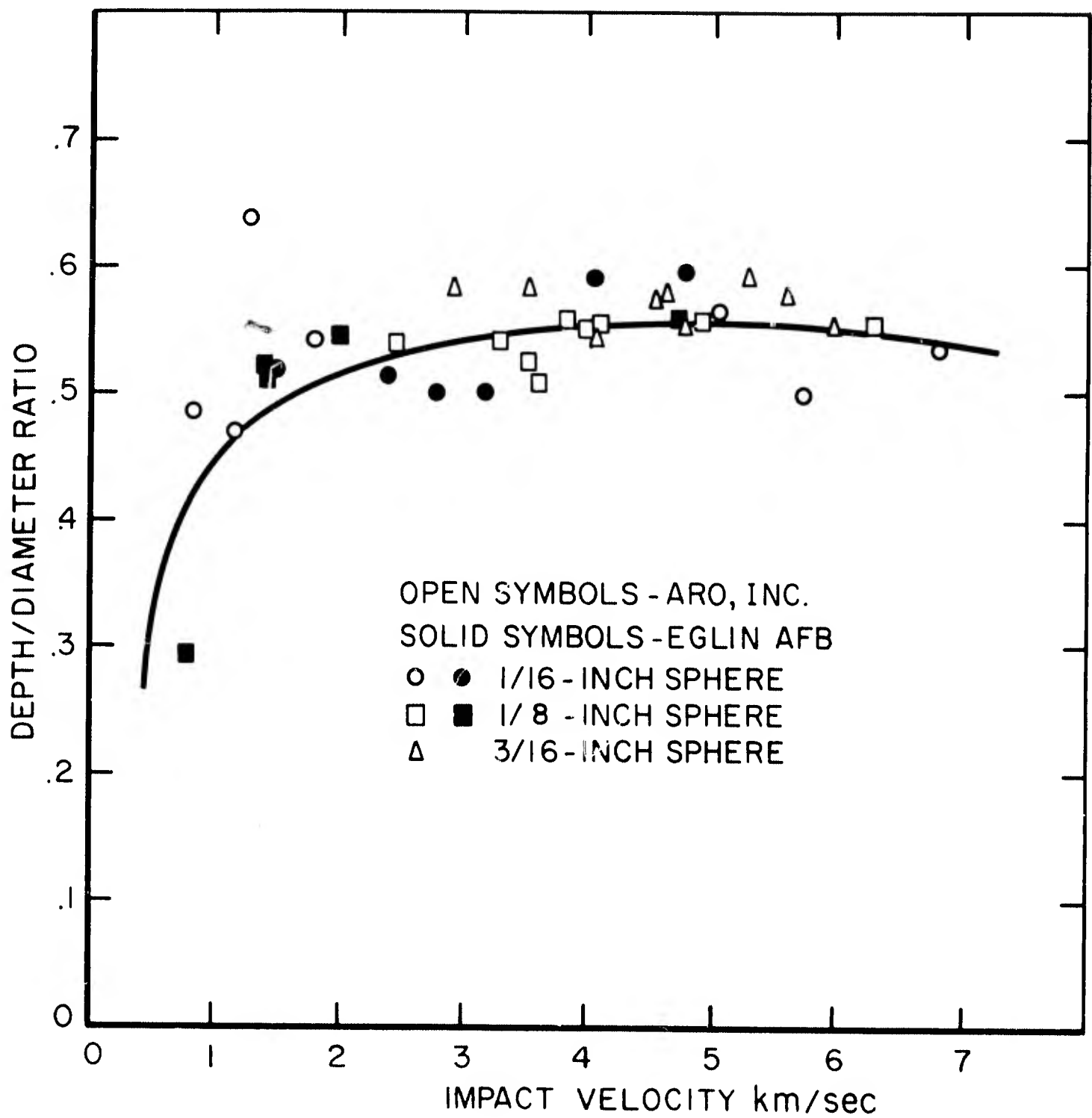
FIGURE 9.   DEPTH/DIAMETER RATIO FOR COPPER SPHERES IMPACTING
COPPER TARGETS

combinations of copper and aluminum are plotted against impact velocity in Figure 10. The curves of Figure 10 suggest four generalities: (1) craters produced by high-density metal spheres impacting low-density metal targets have a depth/diameter ratio greater than 0.5, which means that they resemble hemi-prolate spheroids; (2) craters produced by low-density metal spheres impacting high-density metal targets have a depth/diameter ratio less than 0.5, which means that they resemble hemi-oblate spheroids; (3) craters produced by metal spheres impacting targets of the same metal have a depth/diameter ratio of approximately 0.5, which means that they are nearly hemispherical. In addition, (4) all three curves in Figure 10 show a trend toward the limiting value of 0.5 as was concluded from the plot of Figure 9.

The conclusions that have been drawn suggest that the depth/diameter ratio is a function of material properties at least one of which changes with impact velocity. To obtain some insight into which properties might be involved, the value of the depth/diameter ratio for each projectile-target combination was read from the curves of Figure 10 from a velocity of 1 km/sec through a velocity of 7 km/sec. The empirical values are given in section A of Table 2. The values for the unlike projectile-target combinations were then computed taking the ratio of the identical combinations to be unity. The computed values of the unlike combinations are given in Section B of Tab. 2. Finally, the projectile/target ratio of three material properties (yield strength, acoustic impedance, and density) was determined. These ratios are given in section C of Table 2. The projectile/target acoustic impedance ratio is identical with the inverse ratio of the particle velocities. Comparison of the ratios of section C of Table II with those of section B shows that the yield strength ratio and density ratio are in poor agreement. The elastic wave acoustic impedance ratio (or the inverse particle velocity ratio) is a good fit at an impact velocity of 1 km/sec; it is a progressively less good fit at higher velocities. The acoustic impedance is the product of density and longitudinal wave speed. Both of these properties will take on new and as yet undetermined values in the target and projectile material that has been traversed by the shock waves. This could account for a shift in the value of the ratio as impact velocity is increased. The evidence presented suggests that acoustic impedance may be the material property that affects the depth/diameter ratio of the crater.

Surface and cross-sectional views of craters formed using the four possible projectile-target combinations of copper and aluminum are shown in Figure 11. These craters were formed at the highest or close to the highest impact velocites for which data were collected. Low-velocity craters in the case of copper spheres impacting aluminum targets are distinctly tubular but at high impact velocites the crater

25
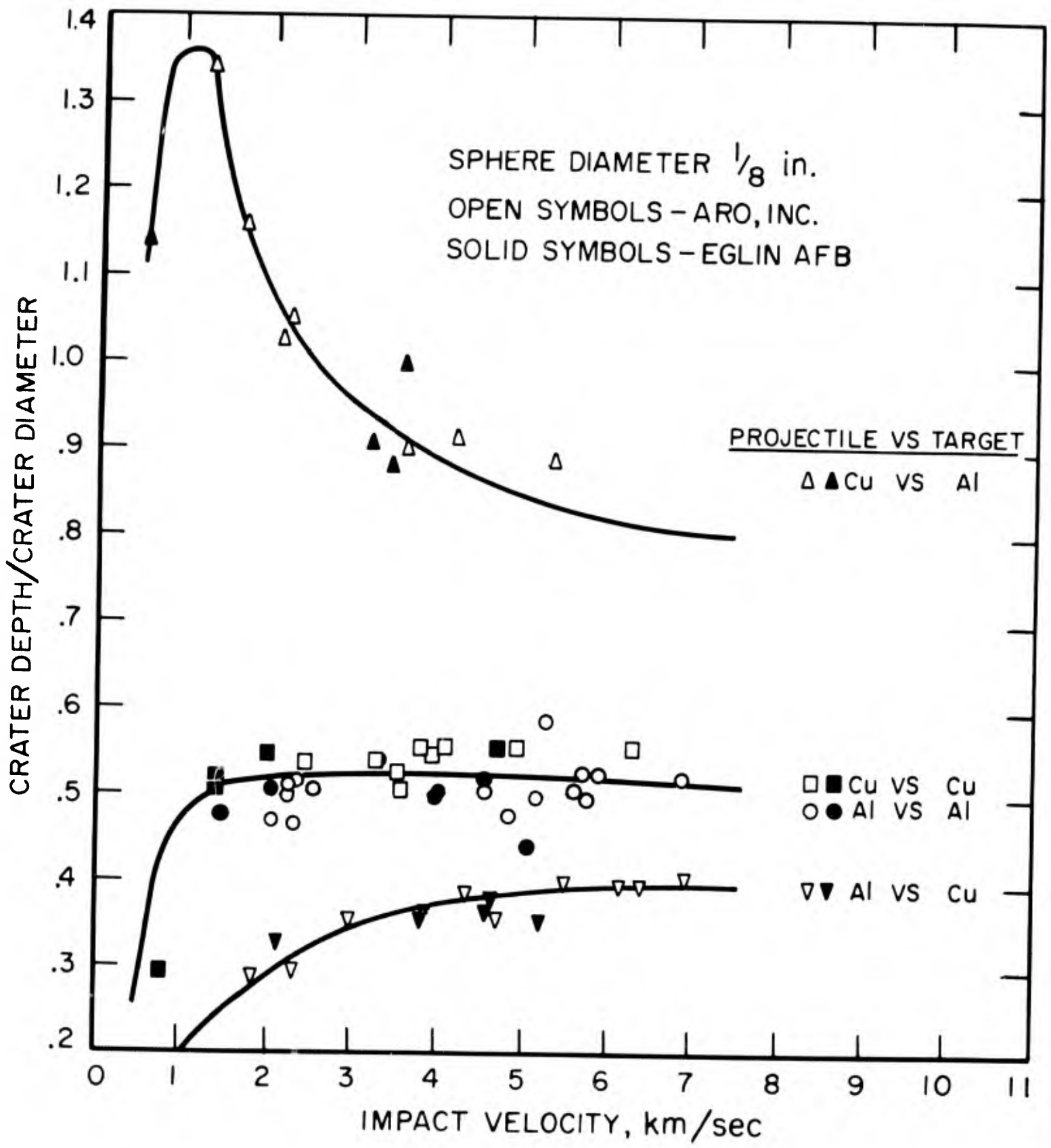
FIGURE 10.   DEPTH/DIAMETER RATIO FOR FOUR
PROJECTILE-TARGET COMBINATIONS

TABLE II

Values of Crater Depth/Diameter Ratio and Ratios of Pertinent Material Properties

A. Depth/Diameter Ratio

Velocity	km/sec	1	2	3	4	5	6	7
Projectile	Target							
Cu	Al	1.36	1.08	0.955	0.89	0.84	0.82	0.81
Cu	Cu	0.48	0.52	0.52	0.523	0.523	0.52	0.515
Al	Al	0.48	0.52	0.52	0.523	0.523	0.52	0.515
Al	Cu	0.20	0.29	0.345	0.37	0.385	0.395	0.40

B. Depth/Diameter Ratio with This Ratio Unity for Identical Combinations

Velocity	km/sec						
Projectile	Target						
Cu	Al	2.83	2.08	1.84	1.70	1.61	1.58	1.57
Cu	Cu	1.0	1.0	1.0	1.0	1.0	1.0	1.0
Al	Al	1.0	1.0	1.0	1.0	1.0	1.0	1.0
Al	Cu	0.42	0.56	0.66	0.71	0.74	0.76	0.78

C. Ratios of Pertinent Material Properties

Combination		Yield Strength	Acoustic Impedance	Density
Projectile	Target	y_p/y_t	z_p/z_t	ρ_p/ρ_t
Cu	Al	4.28	2.47	3.30
Cu	Cu	1.0	1.0	1.0
Al	Al	1.0	1.0	1.0
Al	Cu	0.23	0.41	0.30

CROSS SECTIONAL VIEW

CROSS SECTIONAL VIEW

SURFACE VIEW
ALUMINUM VERSUS ALUMINUM
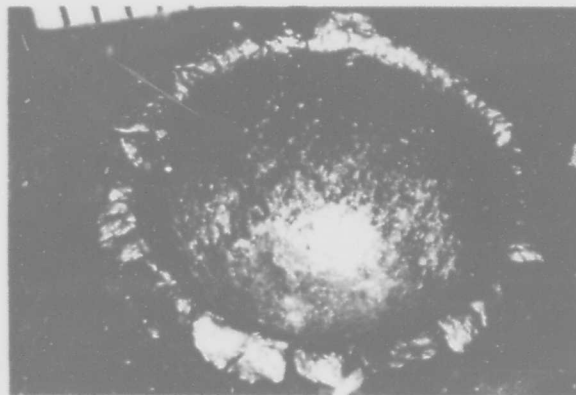
SURFACE VIEW
COPPER VERSUS COPPER

FIGURE 11, SECTION 1. SURFACE AND CROSS-SECTIONAL VIEWS OF
CRATERS FOR FOUR PROJECTILE-TARGET COMBINATIONS

is widened to a shape resembling a hemi-prolate spheroid. It is characterized by a curious step formation; the surface of the steps is coated with copper. Comparison of the surface view with the cross-sectional view (see Figure 11, section 2) reveals that the steps are not concentric rings; they appear as isolated spots in the surface view. A metallurgical investigation of the grain structure around the steps on a cross section of a crater of this kind might reveal information of interest, but time was not available for this study.

There was a residual deposit of the projectile sphere in most of the craters. The method used to determine the depth of the projectile residue in the craters produced by each of the four possible projectile-target combinations of copper and aluminum is described in section 4. The depth of the projectile residue that was found for impacts of 1/8-inch-diameter spheres is plotted against impact velocity in Figure 12. Several interesting facts can be gathered from the plots: (1) The depth of the projectile residue falls rapidly to a negligible value as the impact velocity is increased. After the first minimum depth is reached, however, the depth of the projectile residue appears to rise and fall. Whether it will go to zero in each case cannot be determined from the plot but it is reasonable to assume that this will be the case. (2) The curves for copper spheres impacting copper targets and for aluminum spheres impacting aluminum targets are similar. (3) The curve for copper spheres impacting aluminum targets lies above the similar metal curves and the curve for aluminum spheres impacting copper targets lies below them. This is the same positioning as that found in the plots of depth/diameter ratio against velocity. (4) In the case of aluminum spheres impacting copper targets, the projectile residue is completely negligible after the impact velocity has reached 3.5 km/sec. This fact is explained by the incandescent appearance of the ejecta in the early stages of such an impact; this is described below. The evidence suggests that when an aluminum sphere impacts a copper target at high velocity, the aluminum sphere literally burns up.

Inspection of Beckman and Whitley framing camera pictures of the ejecta from the craters produced by impacts involving the four possible projectile-target combinations of copper and aluminum was informative. Selected views of the impact of a 3/16-inch aluminum sphere against an aluminum plate at 4.727 km/sec (15,510 ft/sec) are shown in Figure 13. From the views of Figure 13, section 1, there appears to be no evidence of incandescence in initial stages of this impact. There is a neck in the structure of the ejecta in these views; below this neck the structure flares outward as it meets the surface of the target. This configuration is characteristic of liquid impacts (see Figure 2). The ejecta appear to consist of coherent streams and resemble the ejecta of the initial phase of a true liquid impact (see Figure 2).

29

CROSS-SECTIONAL VIEW   CROSS-SECTIONAL VIEW
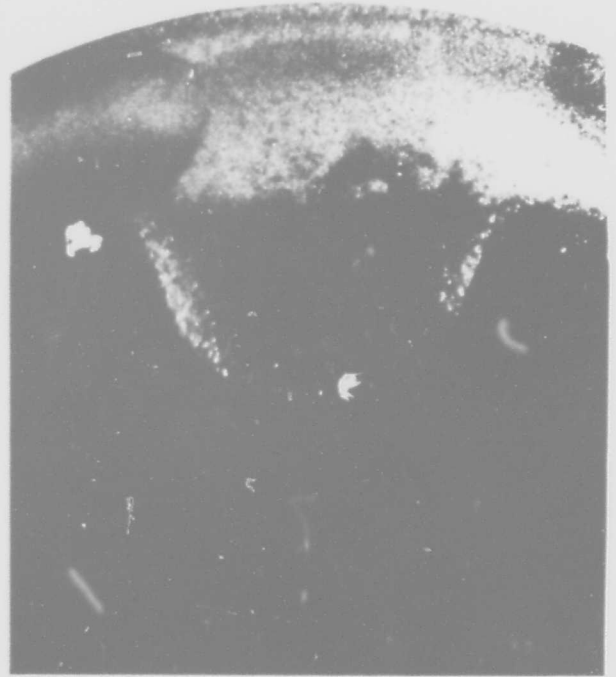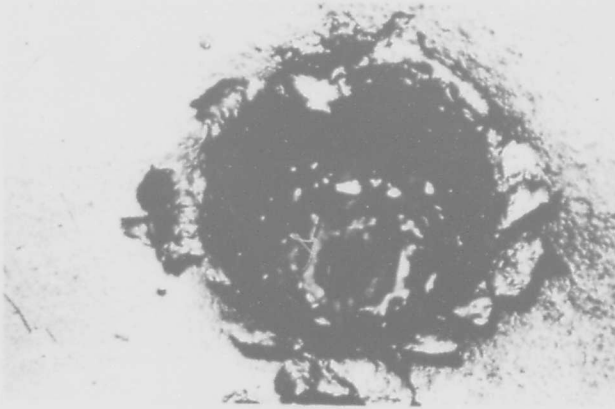
SURFACE VIEW   SURFACE VIEW
COPPER – ALUMINUM   ALUMINUM – COPPER
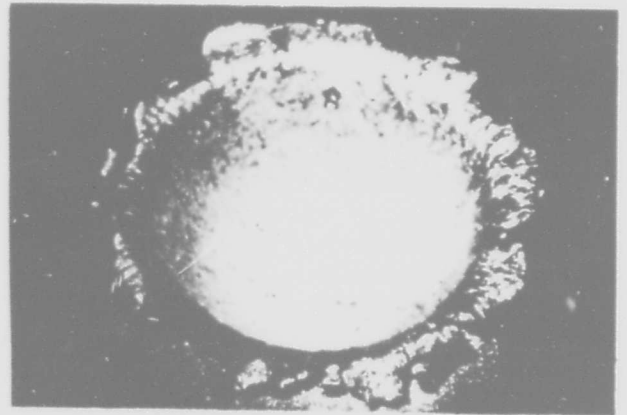
FIGURE 11, SECTION 2.   SURFACE AND CROSS-SECTIONAL VIEWS OF
CRATERS FOR FOUR PROJECTILE-TARGET COMBINATIONS
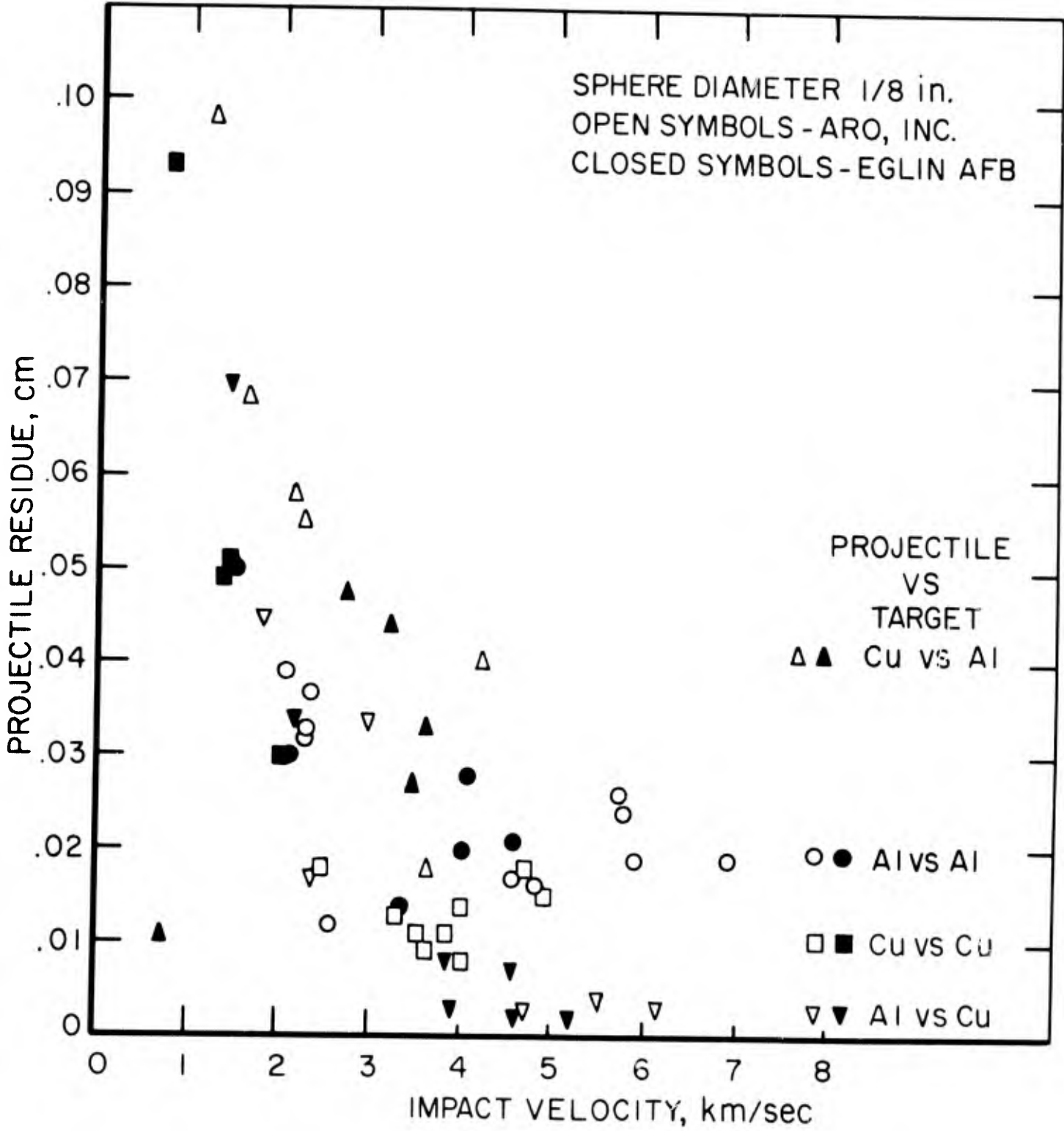
FIGURE 12. VELOCITY DEPENDENCE OF PROJECTILE RESIDUE FOR FOUR
PROJECTILE-TARGET COMBINATIONS
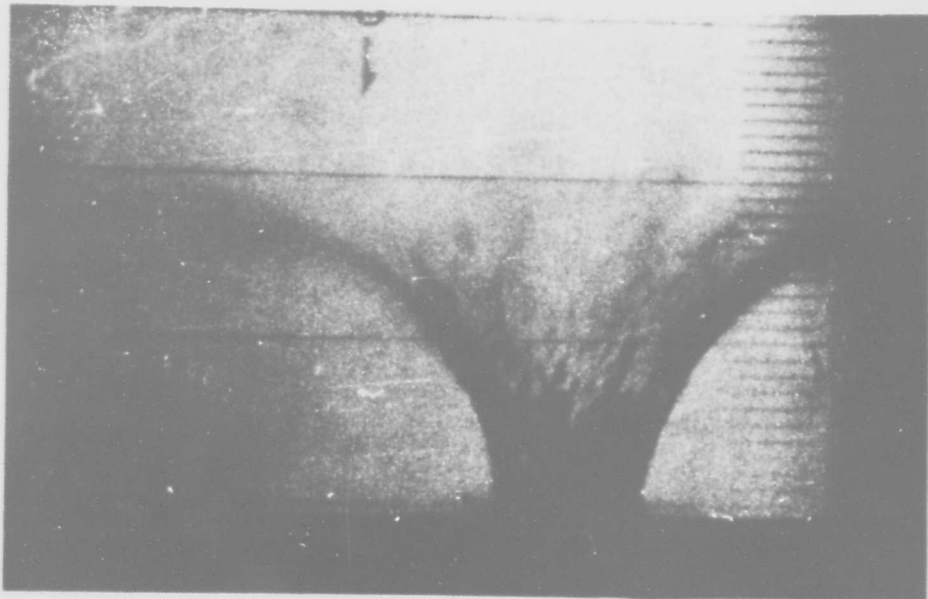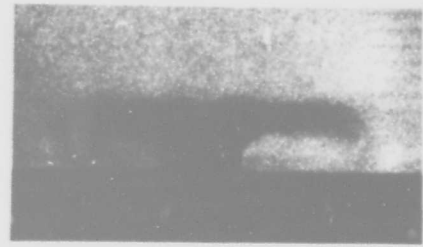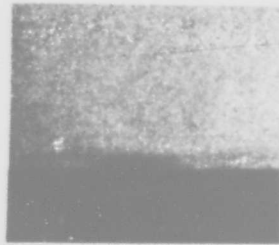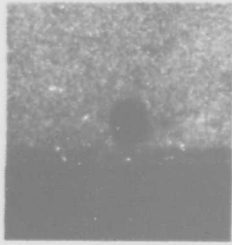
FIGURE 13, SECTION 1.   IMPACT OF A 3/16-in. ALUMINUM SPHERE
AGAINST AN ALUMINUM TARGET AT 4.727 km/sec (15,510 ft/sec)

32

In the bottom view of Figure 13, section 1, discreet particles are visible in the ejecta. The configuration of the particles in the later views shown in Figure 13, sections 2 and 3, suggests that the fluid or quasi-fluid jets or streams may have segmented and broken up into streams of discreet masses. This type of breakup is characteristic of liquid jets; it is a result of instability.

In the later views shown in Figure 13, section 2, the neck in the structure of the ejecta has disappeared and the base of this structure rises at a sharp angle from the surface of the target. Furthermore, pieces of the raised metal structure at the mouth of the crater are breaking away so that the height of this collar-like structure above the target surface is less in the lower view of Figure 13, section 2, than in the upper view; its height is still further reduced in Figure 13, section 3. This seems to be the source of the large masses in the ejecta. The irregular shape of these masses suggests that they are in the solid or in a semi-solid state.

The measured diameter of the crater produced by this impact is 2.273 cm (0.8949 in.) The measured diameter of the neck in the structure of the ejecta in the lower view of Figure 13, section 1, is 2.21 cm (0.870 in.) $\underline{c/}$ This suggests that nearly the full size of the impact crater was reached while the ejecta were in a fluid or quasi-fluid state. This deduction is in agreement with the evidence which suggests that discreet masses in the ejecta are formed by the breakup of fluid or quasi-fluid streams.

The reported volume of the residual crater formed by this impact is 2.867 cm^3 which is equivalent to 7.738 grams of aluminum. Because is requires 10.63×10^9 ergs to heat a gram of aluminum to its melting point and to give it its latent heat of fusion, it would require 8.225×10^{10} ergs to heat and melt the contents of the crater. Because the reported average mass of the 3/16-inch aluminum spheres that were used is 0.1544 grams and because the impact velocity was 4.727 km/sec, the energy delivered by the impact was only 1.724×10^{10} ergs or only enough to melt 0.2096 the contents of the crater.

The evidence just given points to the conclusion that the fluidity being observed is not a true liquefaction but a quasi-fluidity. The quasi-fluidity may be flow of target metal that has such high energy density that it is no longer confined by a crystal lattice, that is, an extreme form of plastic flow.

Incandescence in the first stages of the impact makes its appearance at an impact velocity of about 5.2 km/sec (17,000 ft/sec) both for impacts of 3/16-inch aluminum spheres against aluminum targets and for impacts of 3/16-inch copper spheres against copper targets. That the threshold velocity is the same

33
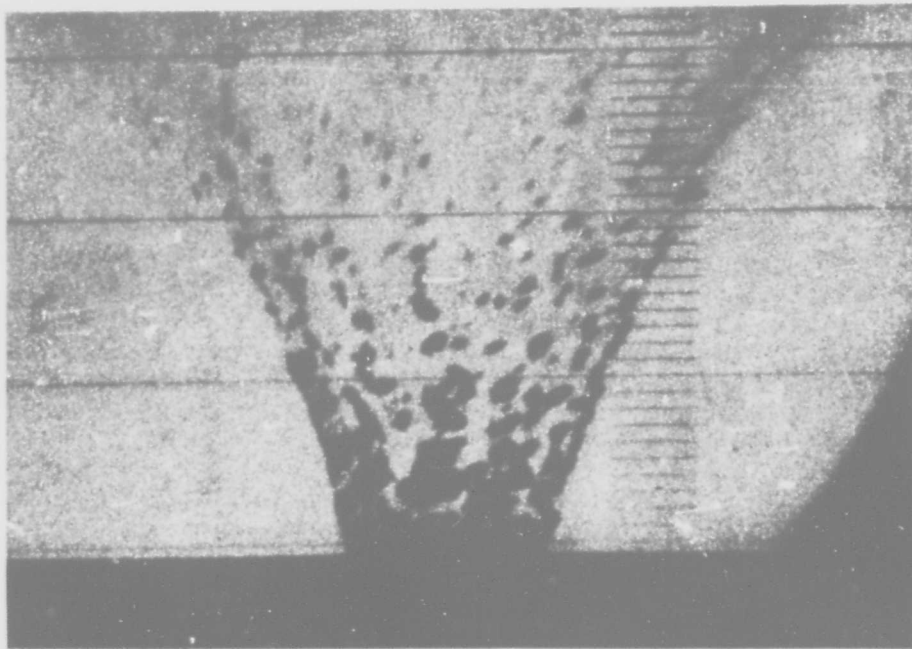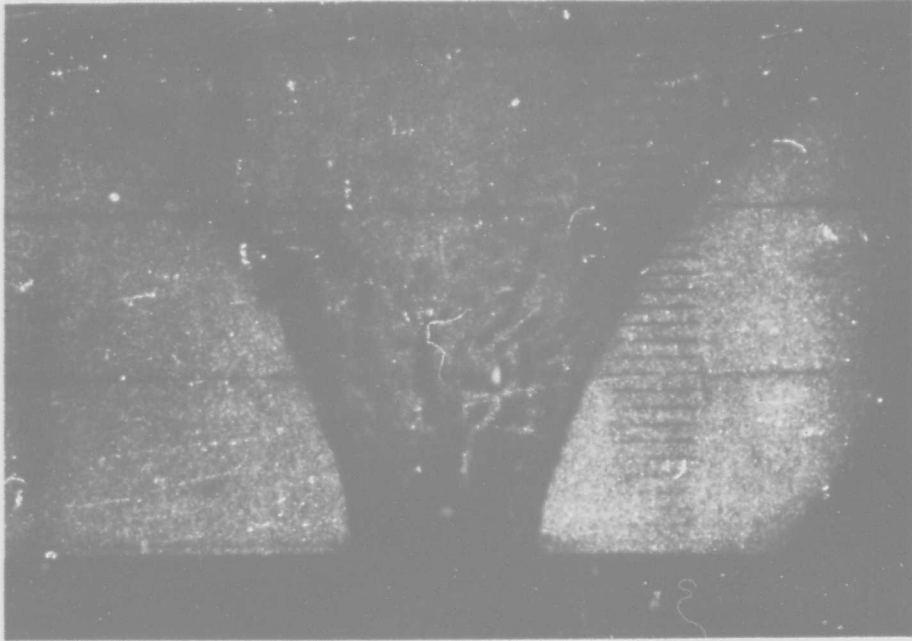
FIGURE 13, SECTION 2. IMPACT OF A 3/16-in. ALUMINUM SPHERE
AGAINST AN ALUMINUM TARGET AT 4.727 km/sec (15,510 ft/sec)

FIGURE 13, SECTION 3. IMPACT OF A 3/16-in. ALUMINUM SPHERE
AGAINST AN ALUMINUM TARGET AT 4.727 km/sec (15,510 ft/sec)

35

for both of these projectile-target combinations is surprising in view of the fact that: (1) the impact energy is roughly three times larger for the copper impact than for the aluminum impact because of the density difference between copper and aluminum, and (2) the energy required per gram to heat and melt aluminum is roughly 50 per cent larger than that required to heat and melt copper. A possible explanation of this may be that aluminum undergoes more plastic flow than copper does and, therefore, may be more efficient in converting impact energy to heat.

The impact of a 3/16-inch copper sphere against a copper target at 5.270 km/sec (17,290 ft/sec) is shown in Figure 14. In the first view of Figure 14, section 1, the sphere is approaching the target; in the second view the impacted sphere is incandescent. The first two views of Figure 14, section 2, show the ejecta as consisting of fluid or quasi-fluid streams. Comparison of Figure 13, section 1, with Figure 14, section 2, shows that the structure of the aluminum ejecta has a more distinct neck than the structure of the copper ejecta has; below this neck it flares outward as it meets the surface of the target.

In this respect the aluminum ejecta resemble the ejecta from a true liquid impact (see Figure 2) more than the copper ejecta do. Olshaber and Bjork [6] have found that the threshold velocities below which liquefaction is not to be expected are 5.0 km/sec for impacts of aluminum against aluminum and 4.4 km/sec for impacts of copper against copper. From the views of Figure 13, section 1, and those of Figure 14, section 2, an aluminum-against-aluminum impact at 4.727 km/sec appears to be more fluid than a copper-against-copper impact at 5.270 km/sec. This evidence confirms further the tentative conclusion that the fluidity which is being observed is not a true liquefaction.

As was observed for the impact of an aluminum sphere against an aluminum target in the views of Figure 13, segmentation of the fluid jets into distinct masses can be seen in the bottom view of Figure 14, section 2, and the breaking away of pieces of the collar-like structure at the mouth of the crater can be see in Figure 14, sections 3 and 4.

Three views from the impact of a 3/16-inch aluminum sphere against a copper target at 5.328 km/sec (17,481 ft/sec) are shown in Figure 15. Impacts with this projectile-target combination at this velocity are distinguished by: (1) strong incandescence in the initial stage, (2) a greater tendency for the structure of the ejecta to spread horizontally than is the case for the other projectile-target combinations of copper and aluminum,
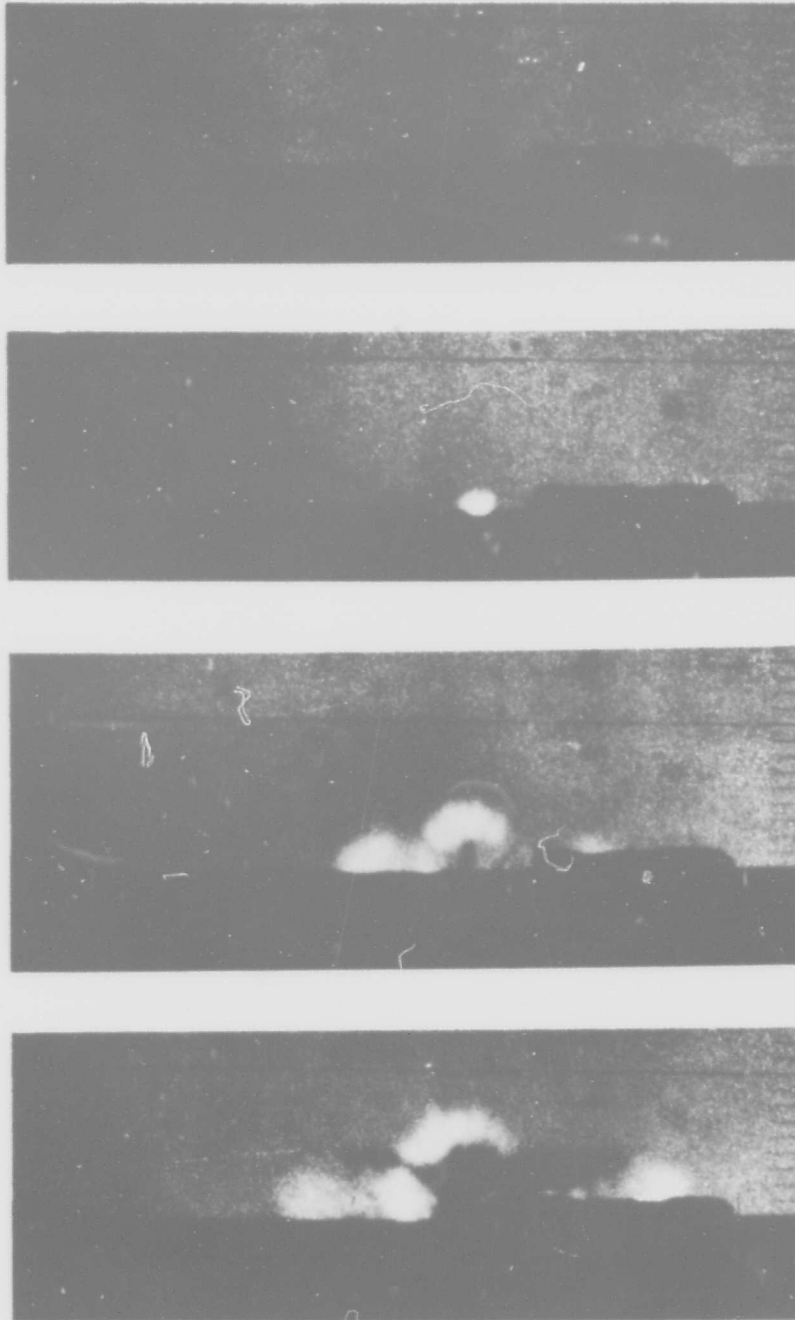
FIGURE 14, SECTION 1.   IMPACT OF A 3/16-in. COPPER SPHERE
AGAINST A COPPER TARGET AT 5.270 km/sec (17,290 ft/sec)
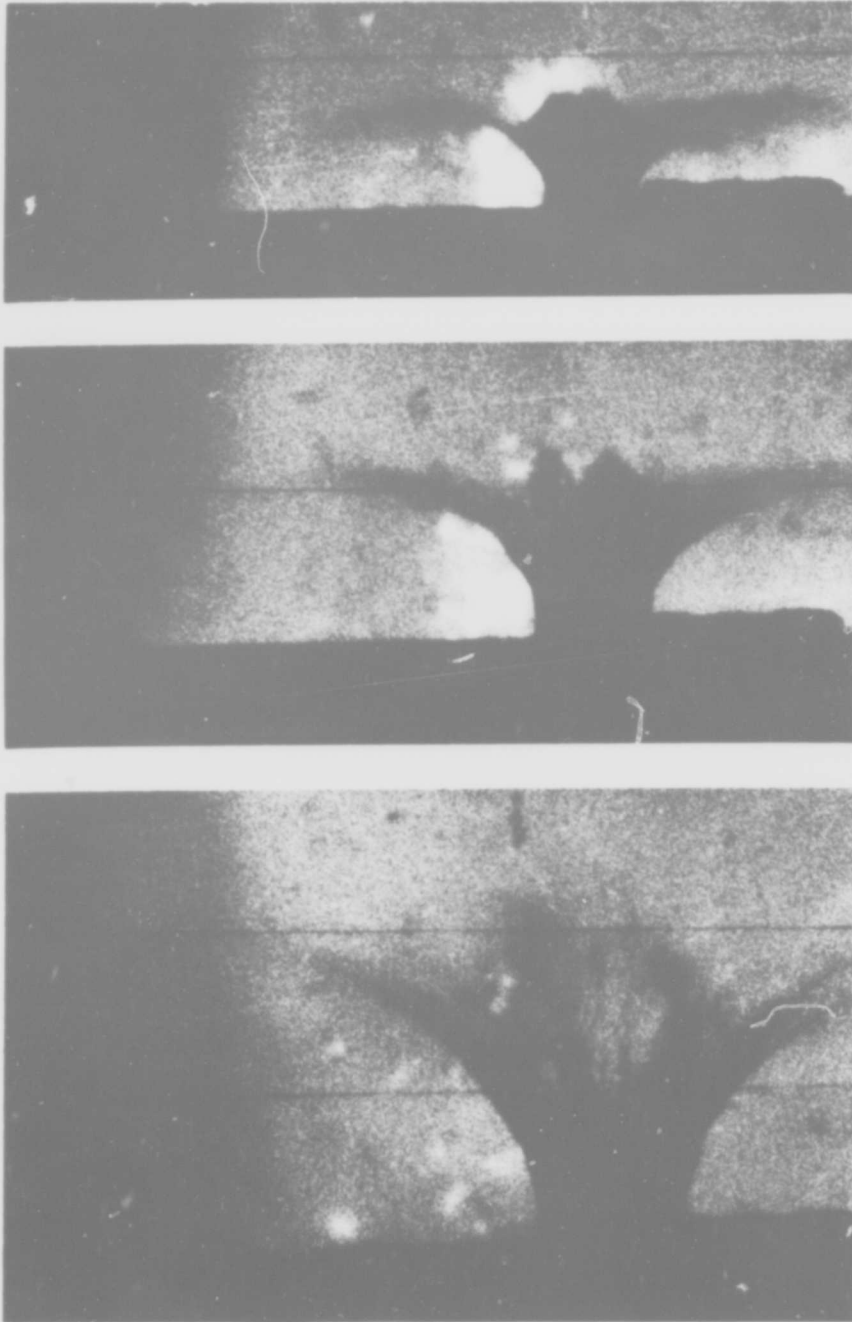
FIGURE 14, SECTION 2.   IMPACT OF A 3/16-in. COPPER SPHERE
AGAINST A COPPER TARGET AT 5.270 km/sec (17,290 ft/sec)
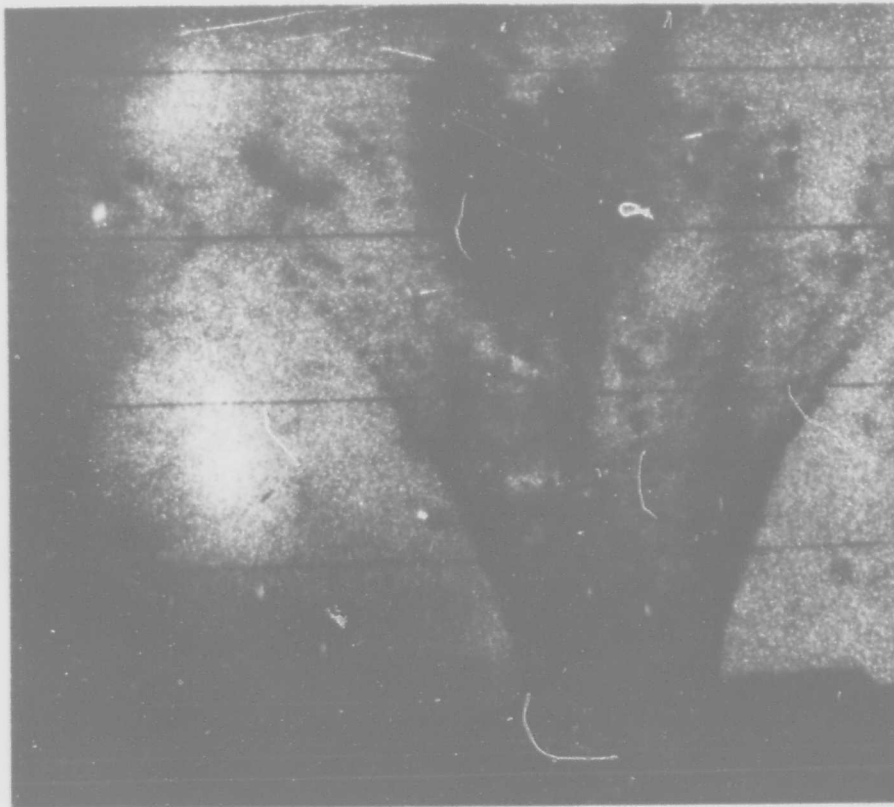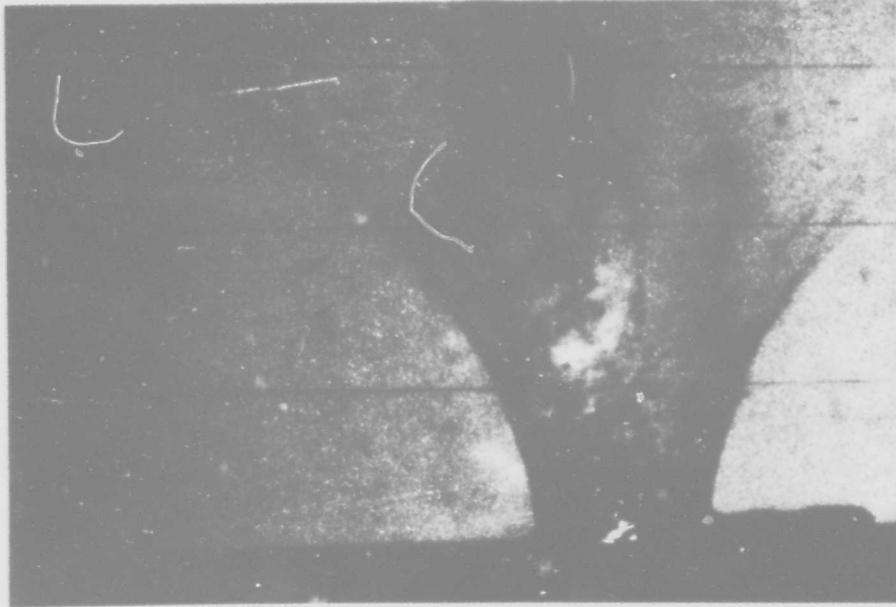
FIGURE 14, SECTION 3.   IMPACT OF A 3/16-in. COPPER SPHERE
ATAINST A COPPER TARGET AT 5.270 km/sec (17,290 ft/sec)

FIGURE 14, SECTION 4. IMPACT OF A 3/16-IN. COPPER SPHERE AGAINST A
COPPER TARGET AT 5.270 km/sec (17,290 ft/sec)
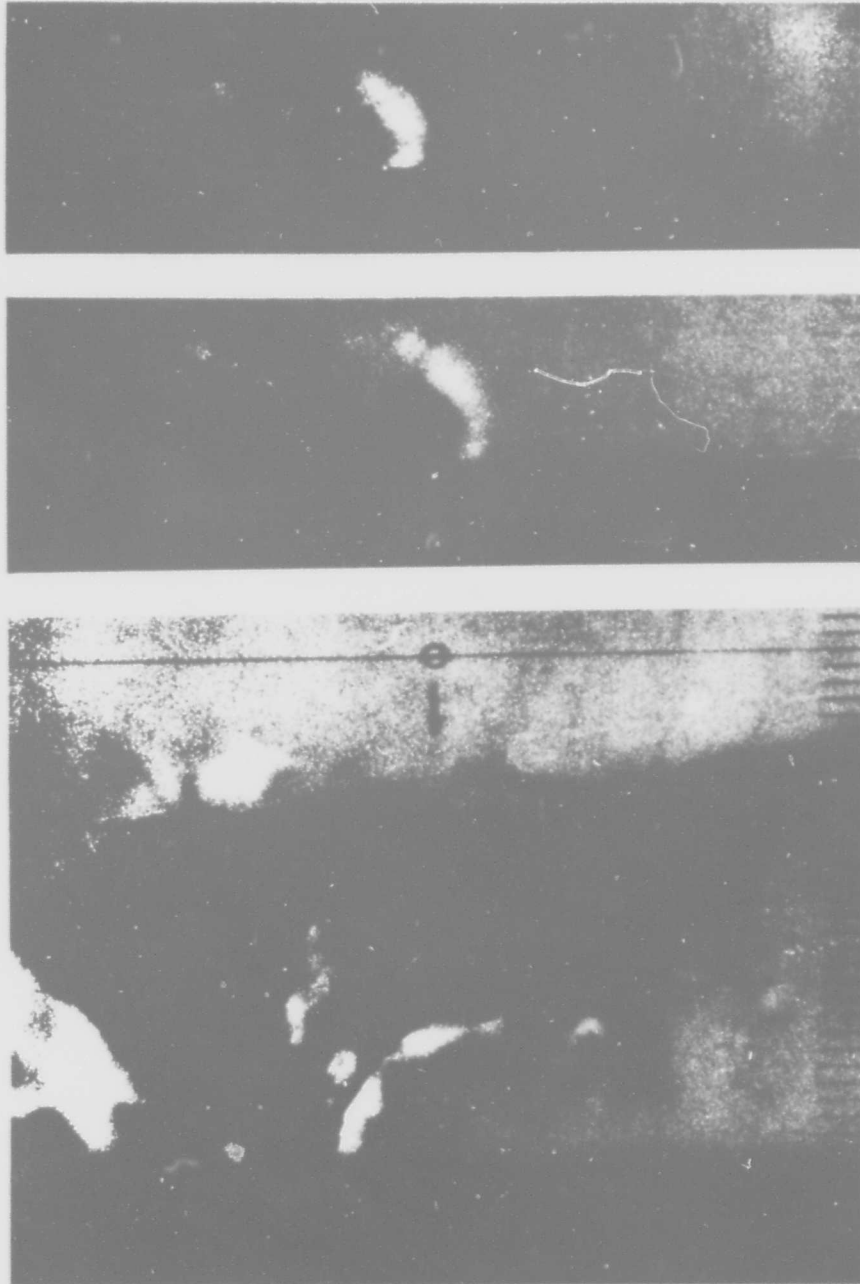
FIGURE 15.   TWO EARLY STAGES AND A LATE STAGE IN THE IMPACT OF
A 3/16-in. ALUMINUM SPHERE AGAINST A COPPER TARGET AT
5. 328 km/sec (17,481 ft/sec)

41

and (3) small rather than large solid masses in the somewhat sparse ejecta. In the light of the fact that the depth of the projectile residue found in the craters for this projectile-target combination was very small (see Figure 12), the strong incandescence produced suggests that an aluminum sphere may be heated to the point of vaporization when it impacts a copper target at about 5.2 km/sec (17,000 ft. sec).

3. Equation for Hypervelocity Crater Depth

3.1 Energy Per Unit Mass of Crater Contents Removed

To gain further insight into the type of flow that may be involved, the energy per unit volume invested in forming the impact crater was studied [d]. In the firings that were made to obtain the experimental data, Mylar screens were unfortunately used to trigger the Beckman and Whitley camera. It is very likely that a projectile sphere, whose surface layer is strongly heated as a result of air friction on passing through the gun, would lose mass on penetrating such a screen. Because small spheres would be more strongly heated than large ones, it was considered that the data for the 1/8-inch and 3/16-inch-diameter spheres would be more reliable than those for the 1/16-inch-diameter spheres.

The impact energy per unit crater volume was determined for impacts of 1/8-inch- and 3/16-inch-diameter spheres at velocities for which the volume of the pellet residue was considered to be negligible in comparison with the crater volume. [e] Because the energy invested per unit mass is the really significant quantity in question, the energy/volume ratios were multiplied by the reciprocal of the target density. The impact energy per unit mass of target metal displaced from the crater is plotted against the impact energy in Figure 16 and best-fit lines have been drawn to the data. The lines of the plots in Figure 16 have a positive slope. The significance of this is that the crater is costing more energy per unit mass of its displaced contents as the impact energy is increased.

From Figure 16 it can be seen that the points for the 1/8-inch spheres and those for the 3/16-inch spheres fall on straight lines that have a different slope. For 3/16-inch spheres, the straight line for impacts of copper spheres against copper targets has the same slope as the straight line for impacts of copper spheres against aluminum targets, but the intercept on the ordinate is different. Similarly, for 1/8-inch spheres, the straight line for impacts of copper spheres against copper targets has the same slope as the straight line for impacts of copper spheres against aluminum targets.

---

[d] This approach was suggested by Dr. George Irvin of the Naval Research Laboratory, Washington, D. C.

[e] The volumes of the craters were measured at the two locations where the hypervelocity firings were made. See section 4.
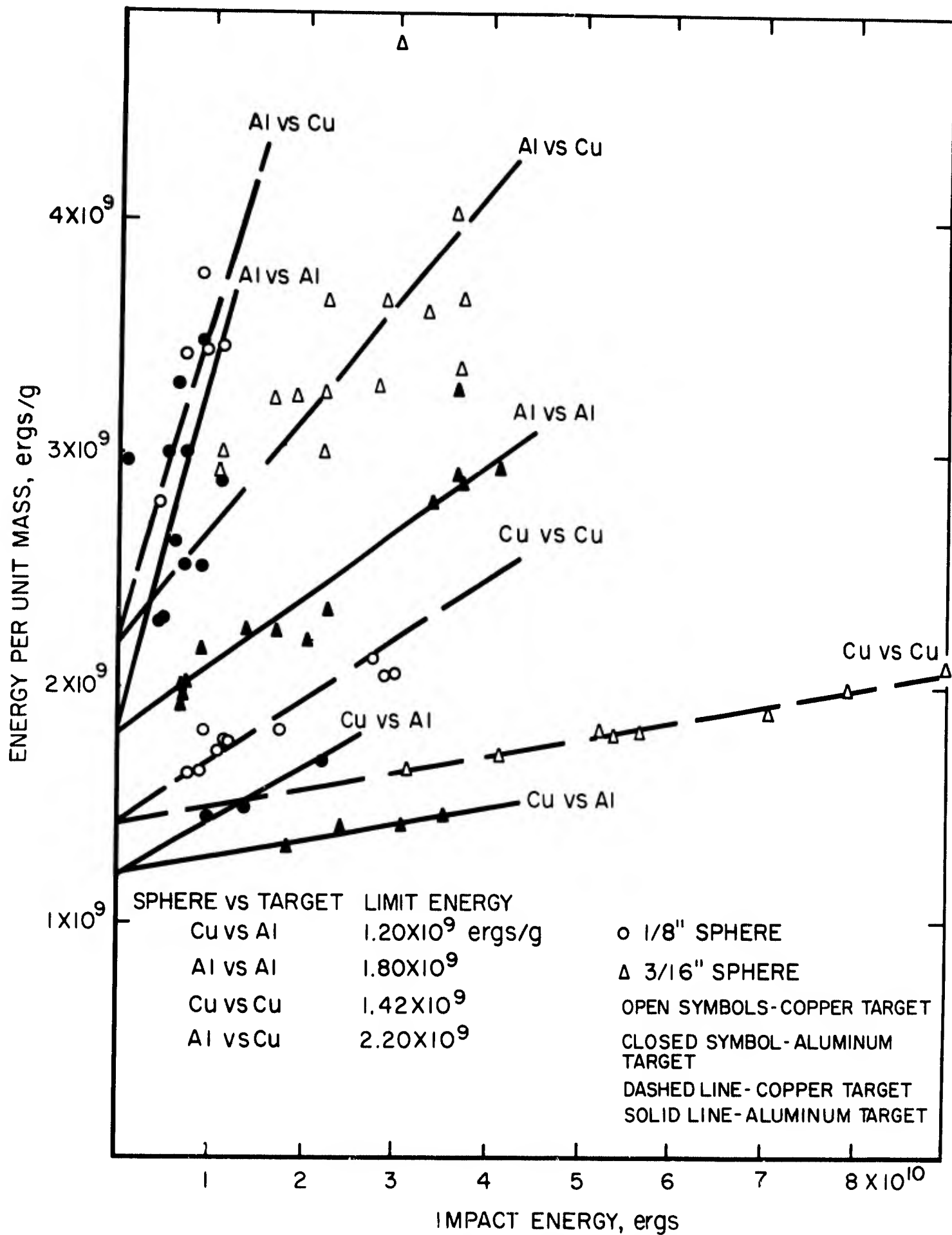
FIGURE 16. ENERGY PER UNIT MASS FOR FOUR PROJECTILE-TARGET COMBINATIONS

The ratio of the slopes of the lines for copper spheres impacting aluminum targets is 0.321 and that of the lines for copper spheres impacting copper targets is 0.292. The inverse ratio of the sphere masses is 0.305 and this suggests that the slope of the line may be inversely proportional to the sphere mass. This supposition is confirmed by the observation that the straight line for impacts of 3/16-inch aluminum spheres against aluminum targets has the same slope as the straight lines for impacts of 1/8-inch copper spheres against both copper and aluminum targets. The reported average mass of the 3/16-inch aluminum spheres that were used is 0.1544 grams and that of the 1/8-inch copper spheres is 0.1546 grams. These masses are essentially identical.

The slope of the lines using copper spheres as projectiles appears to be given by $0.0036/M$ where M is the mass of the impinging sphere. The data using aluminum spheres as projectiles is almost useless for the purpose of this analysis because of the wide scatter in the points. The data for 3/16-inch aluminum spheres impacting aluminum targets have somewhat less scatter than the other data for aluminum spheres. If the straight lines for impacts of copper spheres and that for impacts of 3/16-inch aluminum spheres against aluminum is considered, the slope is given approximately by $0.004/M$.

The significance of the intercept on the ordinate for the plots of Figure 16, which is obtained by extrapolation, is not completely clear. It is an energy per unit mass at zero impact velocity and this suggests that it involves the lattice energy or the activation energy for the quasi-fluid flow that is observed. However, it seems to involve more than this for two reasons: (1) the intercept for a given target material is different when the metal of the impacting sphere is different, and (2) the intercept is larger for copper targets than for aluminum targets which is the reverse of what would be expected if one presumed that the activation energy for the quasi-fluid flow varied as the energy per unit mass required to heat and melt them (see Table III). Because the lines produced by different sphere sizes for a given projectile-target combination converge at the intercept, the intercept is not a function of sphere size.

For spheres of different metals impacting targets of the same metal, the following information can be obtained from Figure 16. The intercept on the ordinate for aluminum spheres impacting aluminum targets is 1.80×10^9 ergs/gram; that for copper spheres impacting aluminum targets is 1.20×10^9 ergs/gram. The ratio of these intercepts for the case that the target is aluminum is 1.5.

44

TABLE III

Properties of Copper and Aluminum

Property	Dimensions	Aluminum	Copper
Melting temperature, T_m	°K	[a] 932	[a] 1,356
Vaporization temperature, T_v	°K	[a] 2,720	[a] 2,855
Heat content $H \frac{T_m}{298.15}$	ergs/g	[a] 6.68×10^9	[a] 4.63×10^9
Heat of melting, H_m	ergs/g	[a] 3.95×10^9	[a] 2.05×10^9
Heat content $H \frac{T_v}{298.15}$	ergs/g	[a] 30.04×10^9	[a] 14.09×10^9
Heat of vaporization, H_v	ergs/g	[a] 108.86×10^9	[a] 47.94×10^9
Density, , at 20°C	g/cm^3	[b] 2.6989	[b] 8.96
Sound speed, C	cm/sec	[c] 6.318×10^5	[c] 4.691×10^5
Acoustic impedance, Z	g/sec·cm^2	[d] 1.705×10^6	[d] 4.203×10^6

[a] D. R. Stull and G. C. Sinke, Thermodynamic Properties of the Elements, A. C. S. No. 18, American Chemical Society, Washington, D. C., 1956

[b] Metals Handbook, 8th Edition, American Society for Metals, Metals Park - Novelty, Ohio, 1961.

[c] Values of sound speed in infinite medium for 1100-0 aluminum and annealed electrolytic tough pitch copper measured in NBS Sound Section, by Carroll Tschiegg.

[d] Product of sound speed and density.

Similarly, the intercept on the ordinate for aluminum spheres impacting copper targets is 2.20 x 10^9 ergs/gram; that for copper spheres impacting copper targets is 1.42 x 10^9ergs/gram. The ratio of these intercepts for the case that the target is copper is 1.6. Exact agreement cannot be expected considering the amount of scatter that exists in the experimental data, but the closeness of the ratios suggests the generalization that for projectile-target combinations of copper and aluminum and using a given target material, 1.5 times as much energy per unit mass is fed into crater formation when the projectile is aluminum than when the projectile is copper. The significance of this appears to be that an aluminum sphere is a less efficient tool for forming impact craters than a copper sphere is.

The particle velocity that is produced in the target metal as the result of an impact should be directly related to crater formation in the target and it is possible that consideration of the particle velocity produced in the target may throw some light on why aluminum spheres are less efficient than copper spheres in forming impact craters. The particle velocity that is given to the target metal that has been traversed by the shock wave produced by the impact would be $Z_p V/(Z_t + Z_p)$ if this shock wave were an elastic plane wave.

The elastic plane wave particle velocity in a copper target is $V/2$ if it is hit by a copper projectile and is 0.2886 V if it is hit by an aluminum projectile. The elastic plane wave particle velocity in a copper target is, therefore, 1.7 times as high when it is hit by a copper projectile than when it is hit by an aluminum projectile. Similarly, the elastic plane wave particle velocity in an aluminum target is $V/2$ if it is hit by an aluminum projectile and is 0.7114 V if it is hit by a copper projectile. The elastic plane wave particle velocity in an aluminum target is, therefore, 1.4 times as high when it is hit by a copper projectile than when it is hit by an aluminum projectile. In each case it is seen that the particle velocity produced in the target is higher if the projectile is copper than if it is aluminum.

Several observations made in section 2.2 suggest that another reason for the inefficiency of aluminum projectiles as compared with copper projectiles may be that more energy is lost as heat in impacting aluminum spheres than in impacting copper spheres. In particular, it was observed that in comparison with copper spheres, aluminum spheres tend to heat up to incandescence at lower impact velocities than would be expected.

If the impacting sphere is heated to the point of incandescence and vaporization, energy, which could have been transmitted to the target when the shock wave in the sphere returns to the impact surface after reflection from the trailing face of the sphere,

46

is irreversibly lost as far as crater formation is concerned.
It is possible that projectile-target combinations in which such
losses occur may be inefficient from the standpoint of crater
formation.

The development of heat is associated with plastic flow and
this suggests that the dynamic strength of the sphere metal and
the particle velocity induced in it may be important parameters
in determining crater forming efficiency. The dynamic yield
strengths of the copper and aluminum that were used are not known.
The static yield strengths given in Table IVindicate that the aluminum
is more subject to flow than the copper and this is in agreement with
the observation made in section 2.2 that the ejecta from the crater
produced by. an aluminum-aluminum impact resemble the ejecta from a
true liquid impact more than the ejecta from the crater produced by
a copper-copper impact do. It is also in agreement with the ob-
servation that the aluminum spheres tend to heat up to incandescence
at lower impact velocities than would be expected when comparison is
made with copper spheres.

The effect of particle velocity can be studied by considering
the elastic plane wave particle velocity in the projectile. If
the shock waves that are produced in hypervelocity impacts were
elastic plane waves, the particle velocity in the projectile would
be given by $Z_t V/(Z_t + Z_p)$. For the impact of an aluminum sphere
against an aluminum target or for the impact of a copper sphere
against a copper target this velocity would be $V/2$, but for the
impact of an aluminum sphere against a copper target 't is 0.7114 V.
Therefore, when an aluminum sphere impacts a copper target the
elastic plane wave particle velocity in the sphere is 1.4 times as
large as when a copper sphere impacts a copper target at the same
velocity. That this is directly related to production of in-
candescence and vaporization in the sphere can be seen from the
observation in section 2.2 that the projectile residue in impacts
of aluminum spheres against aluminum targets at high velocities
is similar in amount to that in impacts of copper spheres against
copper targets but that when an aluminum sphere impacts a copper
target at high velocity it literally burns up.

The effect of the yield strength of the projectile metal may
be separated from the effect of the particle velocity in it by
considering copper-copper impacts and aluminum-aluminum impacts.
The particle velocity in the target and in the sphere is the same
for each of these like-metal impacts. However, it was pointed out
in section 2.2 that both the crater depth and the crater depth/dia-
meter ratio were 10 per cent higher for the copper combination than
for the aluminum combination. In terms of the preceding discussion,
the lower cratering efficiency of the aluminum combination would
appear to be the result of greater transformation of energy into
heat in the sphere as a consequence of the fact that the aluminum
that was used tends to undergo plastic flow at a lower applied stress
than the copper. See Table IV.

47

TABLE IV

Tensile Properties of the Metals Used
in the Experiment

Specimen Material	Yield Strength kg/mm^2	psi	Tensile Strength kg/mm^2	psi	Elongation per cent
Copper	4.704	6,690	20.790	29,570	60.9
Copper	5.343	7,600	21.099	30,010	62.3
Copper	5.322	7,570	20.818	29,610	63.9
Copper	5.090	7,240	20.909	29,740	63.4
Aluminum	1.034	1,470	5.175	7,360	55.2
Aluminum	1.174	1,670	4.936	7,020	55.1
Aluminum	1.378	1,960	4.626	6,580	62.4

For spheres of the same metal impacting targets of different metals the following information can be obtained from Figure 16. For aluminum spheres impacting aluminum targets the intercept on the ordinate is 1.80×10^9 ergs/gram and for aluminum spheres impacting copper targets it is 2.20×10^9 ergs/gram. The ratio, for the case that the spheres are of aluminum, is 1.2. Similarly, for copper spheres impacting aluminum targets the intercept on the ordinate is 1.20×10^9 ergs/gram and for copper spheres impacting copper targets it is 1.42×10^9 ergs/gram. The ratio, for the case that the spheres are of copper, is also 1.2. The fact that the ratios have the same value suggests the generalization that when spheres of a given metal are used in projectile-target combinations of copper and aluminum, 1.2 times as much energy per unit mass is fed into crater formation when the target is copper than when the target is aluminum. It appears that the reason for this should be sought in the particle velocity induced in the target metal as a result of the impact, in the transmission coefficient, which governs the extent to which the shock wave that is induced in the projectile by the impact is transmitted into the target, and in the activation energy required for the quasi-fluid flow that takes place.

As indicated above, the particle velocity that is given to the target metal that has been traversed by the shock wave produced by the impact would be $Z_pV/(Z_p + Z_t)$ if this shock wave were an elastic plane wave. The elastic plane wave particle velocity in a copper target is $V/2$ if it is hit by a copper projectile and is $0.2886\ V$ if it is hit by an aluminum projectile. The elastic plane wave particle velocity in an aluminum target is $V/2$ if it is hit by an aluminum projectile and is $0.7114\ V$ if it is hit by a copper projectile. If the impacting spheres are of aluminum, the ratio of the particle velocity produced in an aluminum target over that produced in a copper target is 1.7. If the impacting spheres are of copper, the ratio of the particle velocity produced in an aluminum target over that produced in a copper target is 1.4. The particle velocity in the target, which is an important consideration in crater formation, is higher in each case considered when the target is aluminum than when the target is copper.

In terms of the particle velocity in the target, from this and from the proceding discussion, maximum cratering efficiency should result from the use of copper spheres and aluminum targets. This is in agreement with what is observed experimentally. Efficiency in crater formation would then appear to vary directly with the particle velocity produced in the target. In view of the tentative conclusion arrived at above that particle velocity in the projectile is associated with loss of energy as heat and hence with inefficiency in cratering, it would appear that cratering efficiency varies inversely with the particle velocity produced in the projectile.

Combining these trends, cratering efficiency varies directly with the particle velocity produced in the target and inversely with the particle velocity produced in the projectile. The quotient of these elastic plane wave particle velocities is simply the quotient of the acoustic impedances, $\left[Z_p \, V/(Z_p + Z_t) \right] \, / \, \left[Z_t \, V/(Z_p + Z_t) \right] = Z_p/Z_t$, and the quotient of the acoustic impedances was found to correlate with the crater depth/diameter ratio in section 2.2.

When the shock wave that is induced in the projectile by the impact moves through the projectile and reflects from its trailing face, it reflects as a tension wave. The particle velocity in the tension wave has the opposite direction from the particle velocity in the initial pressure pulse. When this wave comes back through the projectile and returns to the impact surface, it is partly transmitted into the target and partly reflected back into the sphere. It is possible that the part of this tension wave that transmits into the target serves as a cutoff for the cratering process because the particle velocity in it is opposite in direction to that in the compressed target metal.

If the shock waves that are really produced in hypervelocity impacts were elastic plane waves, the transmission coefficient would be $2 \, Z_t/(Z_t + Z_p)$. For a copper sphere impacting a copper target the transmission coefficient is 1.0, and for a copper sphere impacting an aluminum target it is 0.5772. The ratio of transmission into the copper target over that into the aluminum target is 1.7. For an aluminum sphere impacting a copper target the transmission coefficient is 1.4228 and for an aluminum sphere impacting an aluminum target it is 1.0. The ratio of transmission into the copper target over that into the aluminum target is 1.4. From this standpoint a copper target appears to be less efficient for crater formation than an aluminum target.

The activation energy for the quasi-fluid flow of the target metal must also be an important cratering parameter. This energy is not known. If real liquefaction were involved it would be the sum of the energy required to heat the target metal to its fusion temperature, H, and the latent heat of fusion, . It is possible that the first of these quantities may provide a satisfactory measure of the activation energy for flow without liquefaction.

Properties of copper and aluminum are given in Table 3 and quantities that may be of interest in approximating the intercepts of the plots of experimental data shown in Figure 16 are given in section A of Table V. In section B of Table V the values of several functions are tabulated for the four projectile-target combinations of copper and aluminum. The numerical constants for these functions were selected to make the value of the function the same as the experimental intercept for copper-copper impacts.

TABLE V

Approximate Functions for the Experimental Intercepts

Section A. Pertinent Quantities

Projectile	Target	$Z_t/(Z_t+Z_p)$	$Z_p/(Z_t+Z_p)$	Z_t/Z_p	H ergs/g	$H+$ ergs/g	Y kg/mm^2
Copper	Copper	0.5000	0.5000	1.000	4.63×10^9	6.68×10^9	5.114
Aluminum	Copper	0.7114	0.2886	2.465	4.63×10^9	6.68×10^9	5.114
Aluminum	Aluminum	0.5000	0.5000	1.000	6.68×10^9	10.63×10^9	1.195
Copper	Aluminum	0.2886	0.7114	0.406	6.68×10^9	10.63×10^9	1.195

Section B. Experimental Intercepts and Approximate Functions

Projectile	Target	Experimental Intercept ergs/g	$\dfrac{0.6134 \; H \; Z_t}{(Z_t + Z_p)}$ ergs/g	$\dfrac{0.4251 \; (H+) \; Z_t}{(Z_t + Z_p)}$ ergs/g	$\dfrac{0.5553 \; Y \; Z_t}{(Z_t + Z_p)}$ ergs/g
Copper	Copper	1.42×10^9	1.42×10^9	1.42×10^9	1.42×10^9
Aluminum	Copper	2.20×10^9	2.02×10^9	2.02×10^9	2.02×10^9
Aluminum	Aluminum	1.80×10^9	2.05×10^9	2.26×10^9	0.33×10^9
Copper	Aluminum	1.20×10^9	1.18×10^9	1.30×10^9	0.19×10^9

For the functions involving $\triangle H$ and $\triangle H + \varepsilon$ the numerical constants are dimensionless but for the function involving the yield strength Y the numerical constant has the dimensions of volume. It can be seen from the tabulated values of the functions that the expression 0.6134 $HZ_t/(Z_t + Z_p)$ gives the best representation of the observed intercepts. The values of this function are in good agreement with the observed intercepts for copper projectiles; the values are about 10 per cent in error when the projectile is aluminum. However, because of the scatter in the experimental data obtained with aluminum spheres, the intercepts on the ordinate in Figure 16 for impacts of aluminum spheres could be changed quite a bit. It is noteworthy that the acoustic impedance quotient Z_t/Z_p could not be used as a factor with any of these functions without worsening their agreement with the observed intercepts.

3.2 Equations for Crater Depth

The equation for the straight lines of Figure 16 can be written with the use of the general equation for a straight line and with use of the expressions that are able to represent the experimental slopes and intercepts. Taking the slope to be given by $0.0036/M$, which was obtained from the impacts of copper spheres and is thought to be more reliable than the expression $0.004M$, and taking the intercept to be given by $0.6134\triangle H\, Z_t/(Z_t + Z_p)$, the straight lines of Figure 16 are given by $MV^2/2m = (0.0036/M)\,(MV^2/2) + 0.6134\triangle H\, Z_t/(Z_t + Z_p)$ where M is the mass of the impinging sphere, m is the mass (3) of the target metal displaced from the crater that forms, $\triangle H$ is the heat content per gram of target metal integrated from room temperature to the characteristic fusion point of the metal, and Z is the acoustic impedance (product of longitudinal wave speed and density). From equation (3).

$$m = MV^2/\left[0.0036\, V^2 + 1.2268\, \triangle H\, Z_t/(Z_t + Z_p)\right] \qquad (4)$$

The mass of spherical projectile, in terms of its diameter, d, is given by

$$M = \pi d^3\, \rho_p/6 \qquad (5)$$

and for hemispherical craters, the mass of the crater contents displaced, in terms of the crater depth D, is given by

$$m = 2\pi D^3\, \rho_t/3 \qquad (6)$$

The depth/diameter ratio of the craters was found to correlate with the quotient of the acoustic impedances of the target and projectile metals. Let this quotient be introduced into equation (6) in the following way,

$$m = 2\pi (Z_t D^2/Z_p)\, D\, \rho_t/3. \qquad (7)$$

Recalling that the volume of a hemi-oblate spheroid is $2\pi a^2 b/3$ and that of a hemi-prolate spheroid is $2\pi ab^2/3$ where $\underline{a}$ is the major and $\underline{b}$ the minor semiaxis, it can be seen from equation (7) that when $Z_p > Z_t$ the crater should resemble a hemi-prolate spheroid, when $Z_p < Z_t$ the crater should resemble a hemi-oblate spheroid, and when $Z_p = Z_t$ it should be a hemisphere. Because this is in agreement with what is observed experimentally, equation (7) is considered to be a satisfactory way of taking the crater depth/diameter ratio into account.

Introducing equations (5) and (7) into equation (4), and solving for D produces the equation

$$D = 0.62996 \left[\frac{Z_p P_p / Z_t P_t}{0.0036 V^2 + 1.2268 \Delta H\, Z_t/(Z_t + Z_p)} \right]^{1/3} d\, V^{2/3}$$

(8)

Values of crater depth calculated with use of equation (8) are plotted with the experimental data in Figures 17, 18, 19, and 20. From inspection of each of these sets of curves it appears that equation (8) shows an over-all general agreement with the data and that agreement of equation (8) with the data is better the smaller the sphere size and the lower the impact velocity. Calculation of the curves using .004/M for the slope of equation (3) produces essentially the same result but with slightly worsened agreement with the data at high velocities. From the curves it appears that better agreement with the data might be produced if the values of H were slightly smaller. This suggests that the real activation energy for the quasi-fluid flow may be slightly less than the value of the heat content integrated from room temperature to the fusion temperature. The quasi-fluid flow may occur before the fusion temperature is reached.

For velocities above 6 km/sec, a gradual change-over from quasi-fluidity to true fluidity will occur. One would expect that for these velocities the heat of fusion, $\mathcal{E}$, must be added to ΔH in equation (8) in order to provide the energy required for fusion. However, at these high velocities the importance of the term $0.0036 V^2$ will probably make the inclusion or omission of $\mathcal{E}$ unimportant.

It is noteworthy that the use of ΔH to approximate the activation energy for the quasi-fluid flow that takes place, which appears to be acceptable for pure copper and pure aluminum in the annealed state, will not apply for metals that have an increased strength due to alloying, heat treatment, and other means. However, the strength of metals that is produced in these ways is gradually lost as the temperature of the metal is increased. It is possible that the use of ΔH for the flow activation energy of metals strengthened in these ways may be reliable for heated targets.

Equation (8) should be tested further with experimental crater depth data for the four possible projectile-target combinations of other pairs of pure metals. It is believed that if studies similar to that described in this report were to be made utilizing the four possible projectile-target combinations of other pairs of pure metals, more information of value in clarifying the hypervelocity cratering mechanism would be obtained.

For very high impact velocities the term $1.2268 \Delta H \ Z_t/(Z_t + Z_p)$ in the denominator of equation (8) is small in comparison with the term $0.0036 \ V^2$. To consider equation (8) at velocities higher than those for which data are given in Figure 16 involves an extrapolation which may or may not be reliable. If, for purposes of speculation only, one is presumptious enough to take the limit of equation (8) at infinite impact velocity, one finds

$$\lim_{V \longrightarrow \infty} D \sim 4 \left[Z_p \ \rho_p / Z_t \ \rho_t \right]^{1/3} d. \qquad (9)$$

From equation (9), for the case that the spherical projectile and the target are of the same metal, the limiting value of crater depth is about 4 sphere diameters. However, reliance should not be placed on equation (9) until it is tested with experimental crater depth data obtained at very high impact velocities.

To consider equation (8) at low velocities involves no extrapolation. For impact velocities up to 5 or 6 km/sec, the term $0.0036 \ V^2$ in the denominator of equation (8) is small in comparison with the term $1.2268 \Delta H \ Z_t/(Z_t + Z_p)$. Neglecting the term $0.0036 \ V^2$, equation (8) reduces to the approximate equation

$$D \cong 0.5884 \left[\frac{1}{\Delta H} \frac{Z_p}{Z_t} \frac{\rho_p}{\rho_t} \frac{(Z_t + Z_p)}{Z_t} \right]^{1/3} d \ V^{2/3} \qquad (10)$$

An equation identical with equation (10) except that ΔH is replaced by $\Delta H + \varepsilon$, where is the latent heat of fusion, and the numerical constant is 0.665 was derived before the study of the data given in section 2.2 was completed. The derivation, which was based on a model of partial fusion of the target metal displaced from the crater, is given briefly below.

3.3 Approximate Crater Depth Equation

If similarity exists in the partition of energy for the limited hypervelocity regime in which crater depth varies as the 2/3 power of the impact velocity, then the fraction of the impact energy that is used in fusion may be relatively constant within the regime.

Although this argument is speculative, it suggests that the equality

$$(\text{constant}) \ (\text{available energy}) = (\text{volume melted}) \ P_t \ (\Delta H + \varepsilon)$$

may be a reasonable assumption to make in deriving a crater-depth equation. For hemispherical craters of radius D, use of the assumption given by equation (11) would produce the equality

$$\alpha \ (\ 2\pi D^3 \ P_t/3) \ (\Delta H + \varepsilon) = (\text{constant}) \ (\pi \ P_p \ d^3 \ V^2/12)$$

where α is the fraction of the crater contents that melts. From equation (12),

$$D = (\text{constant}) \ \left[P_p \ d^3 \ V^2/\alpha \ P_t \ (\Delta H + \varepsilon) \right]^{1/3}$$

Equation (13) applies only to hemispherical craters; such craters are formed only if the impacting sphere and the target plate are of the same metal. On introducing the acoustic impedance ratio, which appears to be related to the depth/diameter ratio of hypervelocity craters, into equation (12) one obtains

$$\alpha \ \left[2 \ \pi P_t \ D \ (Z_t \ D^2/Z_p)/3 \right] \ (\Delta H + \varepsilon) = (\text{constant}) \left[\pi P_p \ d^3 \ V^2/12 \right]$$

From equation (14), for projectile-target combinations in which $Z_p = Z_t$, the crater is a hemisphere; for projectile-target combinations in which $Z_p < Z_t$, the crater should resemble a hemi-oblate spheroid; for projectile-target combinations in which $Z_p > Z_t$, the crater should resemble a hemi-prolate spheroid. And from equation (14),

$$D = (\text{constant}) \ (Z_p/Z_t)^{1/3} \left[d^3 \ P_p \ V^2/\alpha \ P_t \ (\Delta H + \varepsilon) \right]^{1/3}$$

To obtain maximum crater depth from equation (15), it is necessary to have an explicit expression for α, the fraction of the crater contents that melts.

It was pointed out in section 1 that crater depth in impacts involving no fluidity ($\alpha = 0$) varies as V^1, that crater depth in impacts involving partial fluidity ($0 < \alpha < 1$) varies as $V^{2/3}$, and that crater depth in completely fluid impacts ($\alpha = 1$) varies as $V^{1/2}$. The amount of fluidity that is produced increases with the impact velocity. However, the velocity range over which crater depth varies as $V^{2/3}$ is further characterized by the empirical finding that crater volume varies as the impact energy and, therefore, as V^2.

Although the absolute amount of fluidity and the crater volume both increase as the impact velocity is increased, it is assumed that in the regime where crater depth varies as $V^{2/3}$ the ratio of the absolute amount of fluidity to the crater volume, that is, the melt-fraction α, has a very small dependence on V, and, for practical purposes, may be regarded as independent of V. If α is essentially

independent of V, α will be a constant for any given projectile-target combination.

If the tension wave that reflects from the bounding surface of the sphere and returns to the impact surface were an elastic plane wave, the ratio of the stress in the transmitted wave to the stress in the returned wave would be $2 Z_t/(Z_t + Z_p)$. Because the amount of fusion of target metal that can occur depends on the extent to which the reflected tension wave that returns to the surface of contact is transmitted into the target, may be some function of the acoustic impedance ratio $Z_t/(Z_t + Z_p)$. If this is the case, it follows that will have different values for different projectile-target combinations.

In the light of the preceding discussion, let it be assumed that

$$\alpha = (\text{constant}) \, Z_t/(Z_t + Z_p). \tag{16}$$

On introducing equation (16) into equation (15) one obtains

$$D = \beta \left[\{1/(\Delta H + \varepsilon)\} (P_p/\rho_t) \{(Z_t + Z_p)/Z_t\} (Z_p/Z_t) \right]^{1/3} d \, V^{2/3} \tag{17}$$

where the constant of proportionality for and the constant that limits the amount of the impact energy that is used in fusion are combined in the numerical constant β. The average value of the constant β, which was found by inserting experimentally observed values of D in equation (17), is 0.665 [f]. Introducing this value of β into equation (17),

$$D = 0.665 \left[\{1/\Delta H + \varepsilon)\} (P_p/P_t) \{(Z_t + Z_p)/Z_t\} (Z_p/Z_t) \right]^{1/3} d \, V^{2/3} \tag{18}$$

The locus of equation (18) is plotted as a dashed line in Figure 17, 18, 19 and 20. The equation is not plotted for impact velocities below 2 km/sec because an equation based on a model involving fusion would not apply for those very low velocities. It can be seen from the plots that the locus of equation (18) is in as good agreement with the data as that of equation (8). In some of the plots the agreement appears to be better than that of equation (8). Equation (18) has too steep a slope at high velocities; this is the result of neglecting the velocity dependence of the investment of energy in crater formation.

As noted above, equation (18) was derived before the study of the hypervelocity data that is reported in section 2.2 was completed. A model involving melting of target metal at velocities below even 4 km/sec is unrealistic in view of the observation cited in section 2.2 that impacts against aluminum have the characteristics of fluid impacts at lower velocities than impacts against copper. This

---

[f] The derivation of equation (18) was presented at the Sixth Hypervelocity Impact Symposium [5]. Due to an error in obtaining the integrated value of H, the value of was incorrectly given as 0.695 at that time.

conclusion also follows from the finding of Olshaker and Bjork [6] that melting could not be expected at the low impact velocities for which equation (18) is seen to give relatively good agreement with the experimental data in Figures 17, 18, 19, and 20. The flow that occurs at velocities below 6 km/sec is a quasi-fluid flow rather than a true fluid flow. If the reasoning used in deriving equation (18) is oriented around a quasi-fluid flow model, it provides a theoretical backgroundfor the derivation of equation (8) that neglects the velocity dependence given by the term $0.004 \ V^2$ and that uses $\Delta H + \epsilon$ for the flow activation energy rather than ΔH.

4. Collection of Experimental Data

An experiment was designed at the National Bureau of Standards to obtain data that would provide a stringent test of a hypervelocity crater depth equation. It called for the collection of cratering data for each of the four possible projectile-target combinations of high purity copper and aluminum. Because a hypervelocity gun was not available at the National Bureau of Standards, arrangements were made to have the firings carried out elsewhere.

The hypervelocity firings were made at two locations. A total of 67 test firings were made at Eglin Air Force Base, Florida, from August 1, 1960, to July 1, 1961. At the end of this period, the hypervelocity projectors and associated equipment used to make the firings were transferred to Arnold Engineering Development Center at Tullahoma, Tennessee, where additional firings were made by ARO-Inc. from July 10, 1961, to June 25, 1962. The launcher and range used in making the test firings have been described [9].

To reduce the number of variables to a minimum, cratering data were collected only for normal impact of metal spheres against the planar surface of edge-supported metal plates. The metals selected for use in the experiment were high-purity aluminum (99.99 per cent aluminum), and oxygen-free high-conductivity copper (99.96 per cent copper).

The metal plates used for targets were of different thicknesses up to 5.08 cm (2 in.) thick. The criterion used in selecting the plate thickness for a given sphere size and impact velocity was that there should be no noticeable bulge on the reverse side of the plate as a result of the impact.

The static tensile properties of the metal were measured at the National Bureau of Standards by Mr. Nesbit L. Carivile. Standard ASTM round tensile specimens were machined, annealed,and tested at very slow rates in a Riehle pendulum hydraulic testing machine. The head speed was 0.0762 cm/min (0.03 in./min) before yield; it was increased to a maximum of 0.381 cm/min (0.15 in./min) after yield.
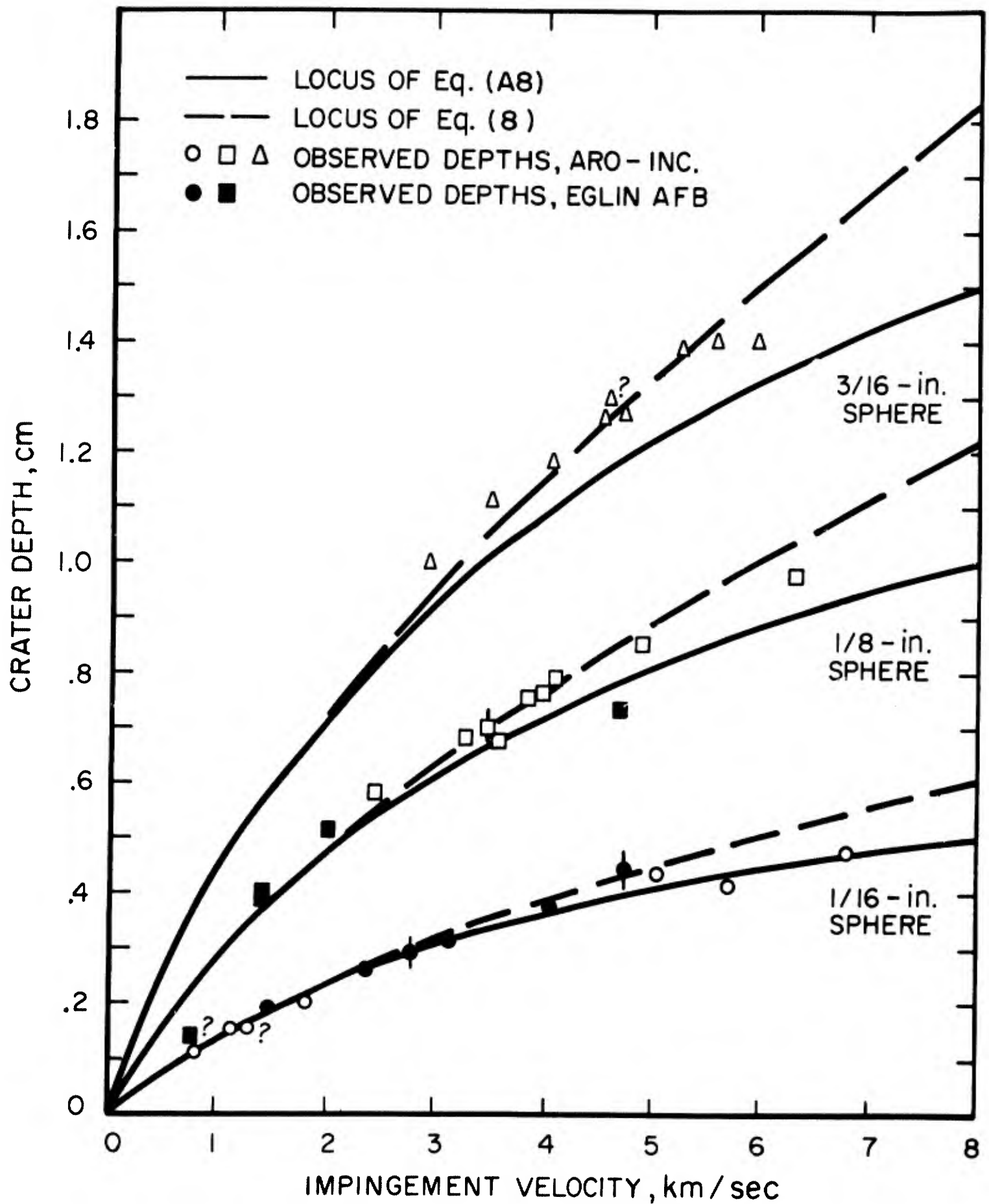
FIGURE 17. CRATER DEPTH PRODUCED IN IMPACTS OF COPPER SPHERES
AGAINST COPPER PLATES
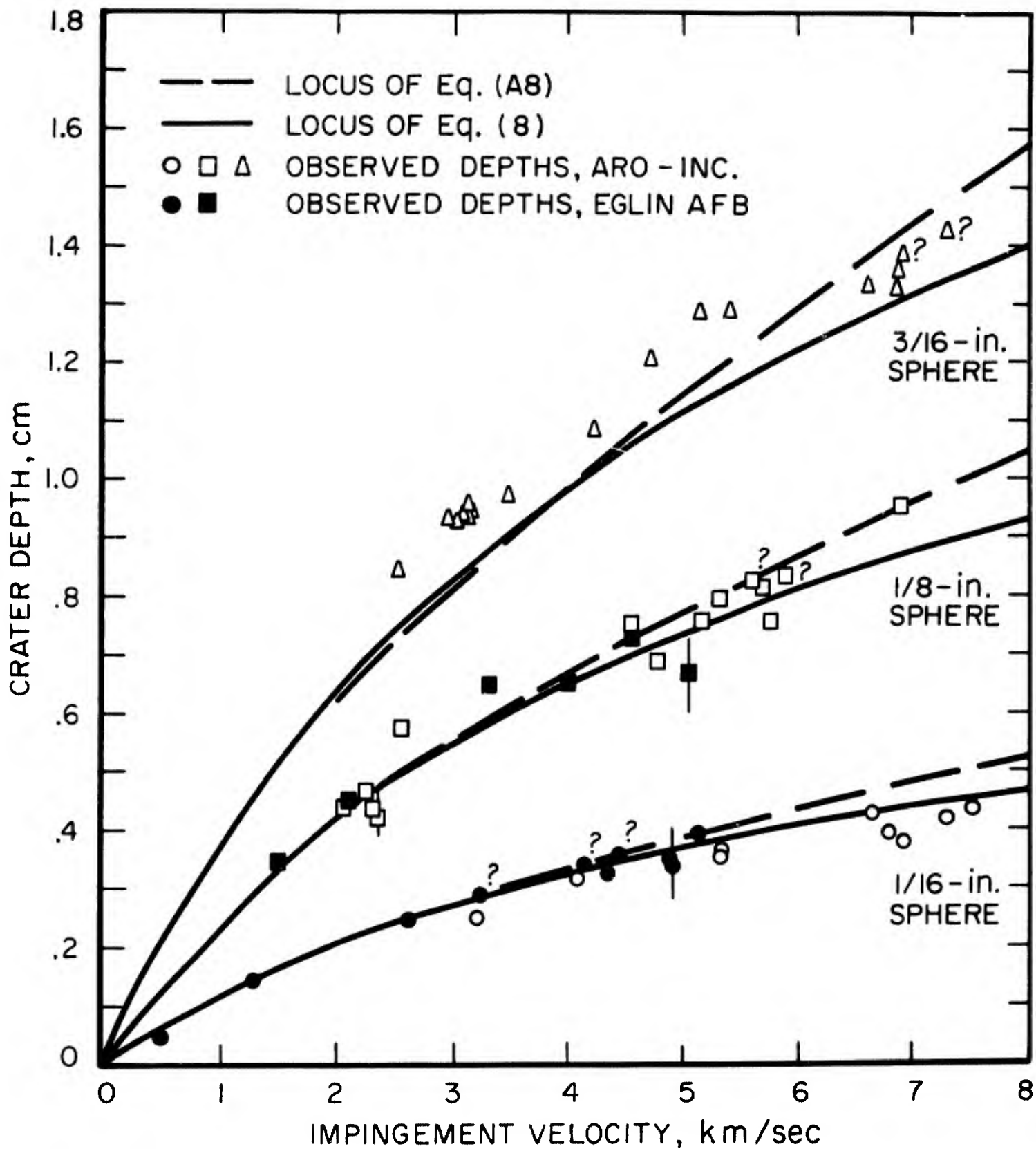
FIGURE 13. CRATER DEPTH PRODUCED IN IMPACTS OF ALUMINUM SPHERES
AGAINST ALUMINUM PLATES
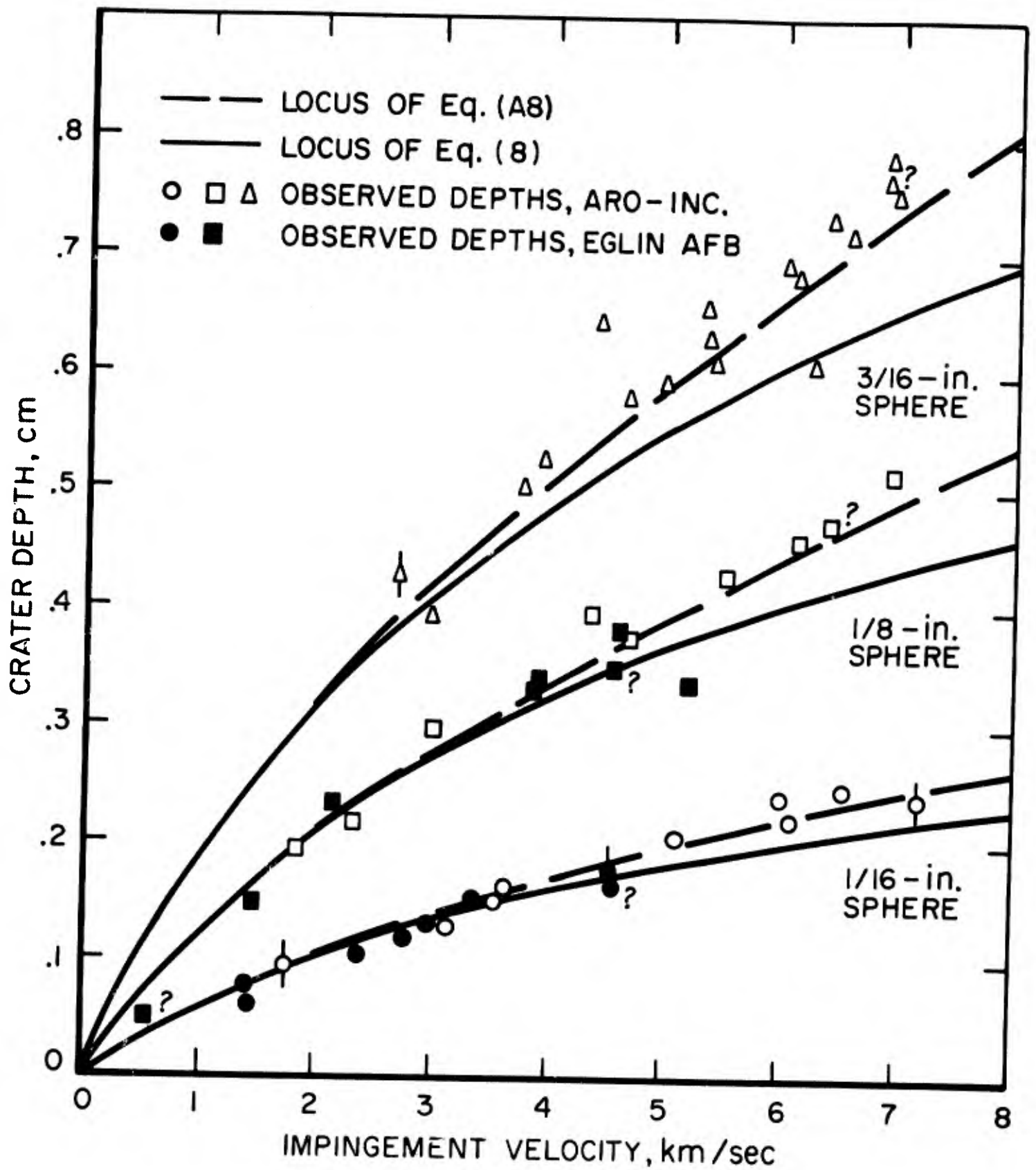
FIGURE 19. CRATER DEPTH PRODUCED IN IMPACTS OF ALUMINUM SPHERES
AGAINST COPPER PLATES
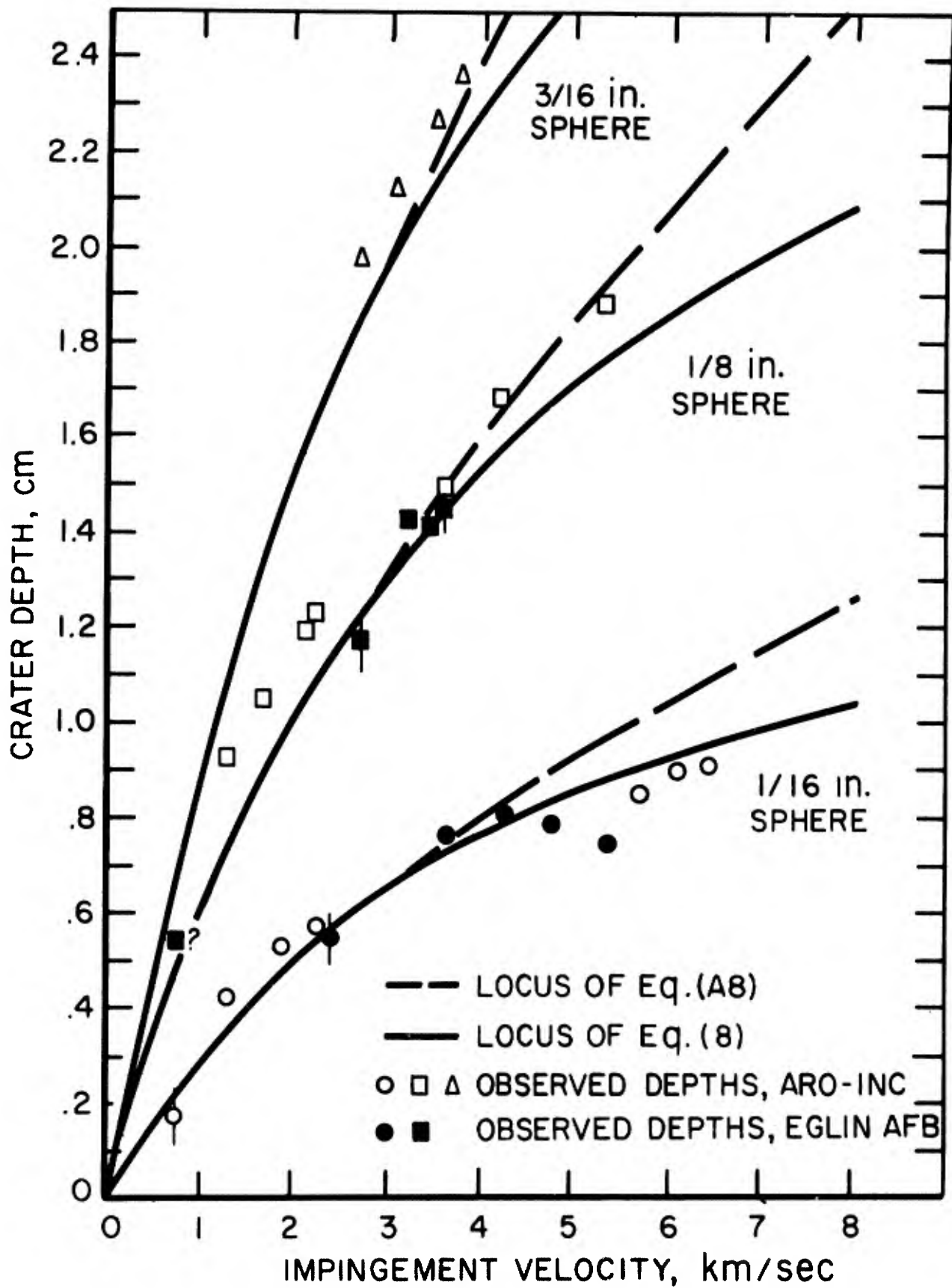
FIGURE 20. CRATER DEPTH PRODUCED IN IMPACTS OF COPPER SPHERES
AGAINST ALUMINUM PLATES

Strain was autographically recorded on a Baldwin-Templin type (solenoid) extensometer. The data obtained were 0.2 per cent offset yield strength, tensile strength, and elongation in 5.1 cm (2 in.). The results of measurements on specimens of each metal are given in Table IV.

The sphere sizes were 0.15875 cm (1/16 in.) diameter, 0.3175 cm (1/8 in.) diameter, and 0.47625 cm (3/16 in.) diameter. The spheres were formed from wire made of the same metals as the target plates. During the course of the firings, the spheres were fabricated by two different manufacturers. The size and weight of the spheres as determined by measurements on samplings at Eglin Air Force Base and at Arnold Engineering Development Center are given in Table VI.

Both the projectiles and targets were annealed to remove work hardening.

All of the firings were made at reduced pressure to prevent ablation of the projectiles as far as feasible. In the firings made at Eglin Air Force Base the target chamber pressure was maintained between 8 and 13 mm of mercury. In the firings made by ARO-Inc. the range pressure was between 1 and 10 mm of mercury.

The impact velocity was determined from Beckman and Whitley camera pictures of the impinging sphere just before it struck the target. The required measurement is the distance travelled by the sphere between consecutive frames. Resolution of the projectile image limits the accuracy with which this distance can be known.

At Eglin Air Force Base the reported velocity was determined for each firing by averaging five film readings made by each of two observers. The observers for each measurement were selected at random from a group of several people. The readings were made with the aid of a Telereader which magnified the 35-mm camera film approximately 10 times. The velocity was calculated by an IBM 7090 computer. Data reduction accuracy was found to be 0.5 per cent. The maximum error of the velocity measurement and reduction system was estimated at 1.5 per cent of the reported velocity.

At ARO-Inc. the distance of travel from a reference point was measured for a series of frames using an optical comparator, Recordak microfilm reader, or Fairchild reader. The data were fitted by the method of least squares to a linear curve by a machine program which yielded standard error of fit and velocity. It was estimated that the errors involved in the determination of time and distance allowed an absolute velocity determination within 1 per cent.

Crater depth was measured at Eglin Air Force Base with a depth micrometer having an accuracy of $\pm$ 0.00127 cm ($\pm$ 0.0005 in.). Only one reading was made for each crater. At ARO-Inc. the crater depth

TABLE VI

Size and Weight of Spherical Projectiles Used
in the Experiment

Nominal Size	Material	Diameter cm	Weight g	Source of Measurement
1/16 in.	Aluminum	0.157	0.005115	Eglin AFB
1/16 in.	Aluminum, group I	0.153	0.00519	ARO-Inc.
1/16 in.	Aluminum, group II	0.157	0.00560	ARO-Inc.
1/8 in.	Aluminum	0.326	0.046420	Eglin AFB
1/8 in.	Aluminum, group I	0.320	0.04636	ARO-Inc.
1/8 in.	Aluminum, group II	0.320	0.04660	ARO-Inc.
3/16 in.	Aluminum, group III	0.477	0.15440	ARO-Inc.
1/16 in.	Copper	0.159	0.017780	Eglin AFB
1/16 in.	Copper, groups I and II	0.156	0.01778	ARO-Inc.
1/8 in.	Copper	0.320	0.145440	Eglin AFB
1/8 in.	Copper, group I	0.315	0.14535	ARO-Inc.
1/8 in.	Copper, group II	0.320	0.15460	ARO-Inc.
3/16 in.	Copper, group III	0.476	0.50620	ARO-Inc.

was determined with use of an optical depth micrometer. It was reported that the depth measurements were repeatable to within ± 0.0005 cm (± 0.000197 in.). The depth measurements made at both Eglin Air Force Base and at ARO-Inc. were repeated at the National Bureau of Standards using a dial gage. The dial gage was calibrated in NBS Engineering Metrology Section where it was found that the maximum error in the dial indication of the movement of the plunger between any two random positions did not exceed ± 0.003 to 0.004 cm (± 0.00118 to 0.00157 in.) and that the error in dial indication of the movement of the plunger from the zero position did not exceed +0.002 to +0.003 cm (+0.000787 to +0.00118 in.) at some positions or -0.001 to -0.002 cm (-0.000394 to -0.000787 in.) at other positions at 20°C (68°F).

After the crater depth measurements made at Eglin Air Force Base and at ARO-Inc. were repeated at the National Bureau of Standards, the craters were cut into two pieces in order to determine the depth of the projectile residue that remained in the crater. The cuts were made a little to one side of the center of the crater; the larger section was mounted in plastic. The mounted cross sections were then abraded until the depth of the crater in cross section was close to the depth of the crater that was measured before cutting it. The mounted cross sections were given a metallurgical polish and the depth of the projectile residue in the crater was measured with a machinist's microscope.

The projectile residue was easily discernible in the craters formed by impact of aluminum spheres against copper targets and in those formed by impact of copper spheres against aluminum targets. For impacts in which the sphere and target were of the same metal it was necessary to bring the cross section to a high polish and etch it to bring out the crack between the projectile residue and the target material. A photograph of the projectile residue found by this technique is shown in Figure 21. In a small number of cases, it proved impossible to find the separating crack and in these cases the projectile residue could not be measured. The work of measuring the apparent depth of the craters at the National Bureau of Standards and the work of mounting and polishing the crater cross sections and measuring the projectile residue was done by Mr. Raymond L. Hebert and Mr. David P. Dowd.

The real depth of the craters is their apparent depth before sectioning plus the depth of the residue of the sphere material found in them. The apparent crater depth that was measured before the craters were sectioned, the depth of the projectile residue found in the craters, and the real depth of the craters is given in Table VII. The apparent crater depth given is the average of the value found by the investigators at Eglin Air Force Base or at ARO-Inc. and the value found at the National Bureau of Standards. The real crater depths are plotted against the impact velocity in Figures

64
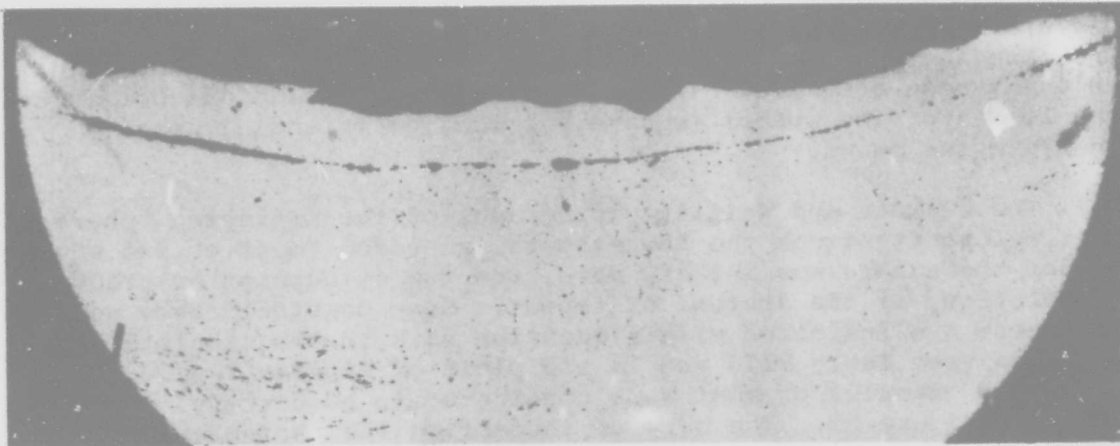
A. PHOTOMICROGRAPH OF CRACK BETWEEN PROJECTILE RESIDUE AND TARGET
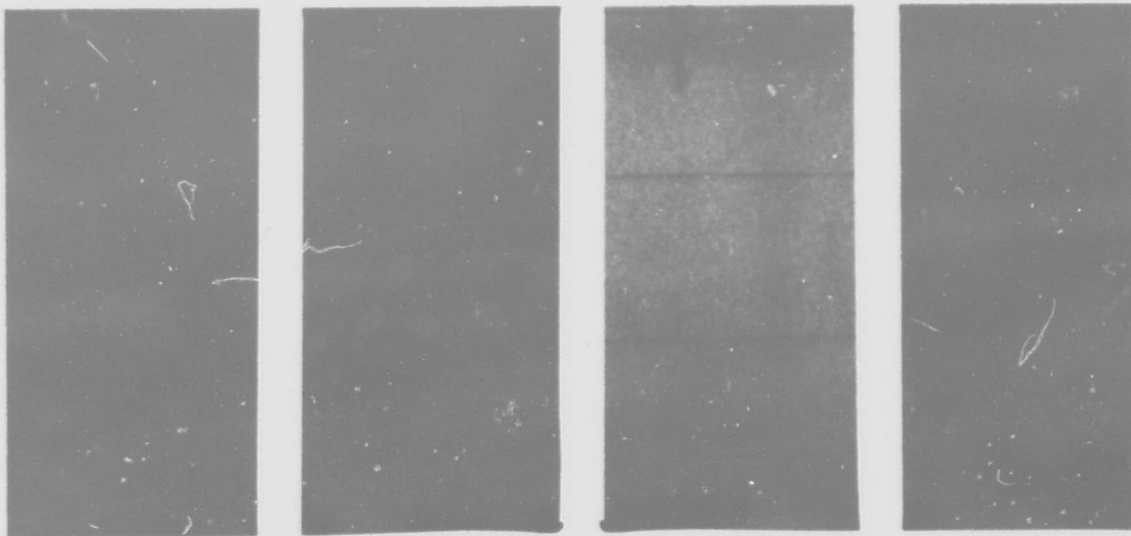
B. EXAMPLES OF SPHERES THAT MAY HAVE LOST WEIGHT BY ABLATION
BEFORE IMPACT.

FIGURE 21. EXAMPLES OF PROBLEMS IN DATA COLLECTION

17, 18, 19, and 20. In a few cases, the two values of apparent crater depth that were averaged were widely different. In these cases a vertical line is drawn through the point on the graphs to indicate the limits of real depth that would have been found had they not been averaged. In most cases the variation did not exceed the limits of the symbol (square, circle, or triangle) used to indicate the point.

The Beckman and Whitley photographs of the impinging sphere just before it struck the target were inspected to determine whether or not the sphere was intact, both from the standpoint of fracture and of ablation, at the instant of impact. Some doubtful cases were found and these are indicated with a question mark in the tabulation of the data (see Table VII) and in the plots of Figures 17, 18, 19, and 20. Some examples of what were considered to be doubtful cases are shown in Figure 21. The work of inspecting the photographs and spotting the doubtful cases was done by Mr. Raymond L. Hebert.

5. Central Protuberance in Lunar Craters

In concluding, a comment should be made in regard to the suggestion [10] that the central protuberance in lunar craters may be the counterpart of the upward-moving jet that forms in the bottom of cavities produced in liquids by the impact of a liquid drop. The upward-moving jet is formed by the recoil of the target liquid; the mechanism is shown graphically in Figure 3.

In order to form an upward-moving jet at the bottom of a hypervelocity crater, there would have to be a high degree of fluidity of the target metal around the crater walls for a sufficiently long period of time. Some evidence, which suggested that the upward moving jet was forming in hypervelocity craters, was reported earlier [11] ; the observation cited has since proved to be an artifact. It is possible that the conditions necessary for formation of this jet may be realized at higher impact velocities.

TABLE VII

Summary of Hypervelocity Crater Depth Data

Section (1) Copper Sphere Impinging Against Copper Plate at Normal Incidence

Source	Impact Velocity km/sec	Apparent Depth Eglin or ARO cm	Apparent Depth NBS cm	Apparent Depth Average cm	Sphere Residue cm	Real Depth cm
— — — — — — — — — — — — — —Sphere Diameter 1/16 in. — — — — — — — — — — — —						
ARO-Inc.	0.806	0.061	0.066	0.063	0.052	0.115
ARO-Inc.	1.146	0.128	0.124	0.126	0.029	0.155
ARO-Inc.	1.289	0.109	0.125	0.117	0.037	0.154
Eglin AFB	1.468	0.168	0.168	0.168	0.024	0.192
ARO-Inc.	1.798	0.182	0.186	0.184	0.022	0.206
Eglin AFB	2.373	0.264	0.248	0.256	0.011	0.267
Eglin AFB	2.766	0.254	0.305	0.280	0.015	0.295
Eglin AFB	3.156	0.300	0.324	0.312	0.007	0.319
Eglin AFB	4.030	0.363	0.367	0.365	0.012	0.377
Eglin AFB	4.752	0.399	0.463	0.431	0.015	0.446
ARO-Inc.	5.038	0.425	0.412	0.418	0.022	0.440
ARO-Inc.	5.716	0.419	0.412	0.415	-	0.415
ARO-Inc.	6.775	0.484	0.470	0.480	-	0.480
— — — — — — — — — — — — — -Sphere Diameter 1/8 in. — — — — — — — — — — — —						
Eglin AFB	0.782	0.048	0.049	0.048	0.093	0.141
Eglin AFB	1.408	0.348	0.336	0.342	0.049	0.391
Eglin AFB	1.425	0.343	0.359	0.351	0.051	0.402
Eglin AFB	2.006	0.488	0.487	0.488	0.030	0.518
ARO-Inc.	2.448	0.573	0.565	0.569	0.018	0.587
ARO-Inc.	3.287	0.688	0.651	0.670	0.013	0.683
ARO-Inc.	3.518	0.716	0.669	0.693	0.011	0.704
ARO-Inc.	3.583	0.671	0.667	0.669	0.009	0.678
ARO-Inc.	3.833	0.749	0.745	0.747	0.011	0.758
ARO-Inc.	3.978	0.758	0.748	0.753	0.014	0.767
ARO-Inc.	4.088	0.788	0.785	0.782	0.008	0.790
Eglin AFB	4.718	0.714	0.717	0.716	0.018	0.734
ARO-Inc.	4.908	0.843	0.841	0.842	0.015	0.857
ARO-Inc.	6.304	0.984	0.970	0.977	-	0.977
— — — — — — — — — — — — — Sphere Diameter 3/16 in.- — — — — — — — — — — —						
ARO-Inc.	2.926	0.996	1.005	1.001	-	1.001
ARO-Inc.	3.520	1.092	1.101	1.097	0.018	1.115
ARO-Inc.	4.038	1.184	1.184	1.184	-	1.184
ARO-Inc.	4.538	1.256	1.254	1.255	0.010	1.265
ARO-Inc.	4.605	1.292	1.287	1.289	0.011	1.300
ARO-Inc.	4.736	1.260	1.282	1.271	-	1.271
ARO-Inc.	5.270	1.391	1.390	1.390	-	1.390
ARO-Inc.	5.586	1.387	1.420	1.403	-	1.403
ARO-Inc.	5.967	1.394	1.424	1.409	-	1.409

TABLE VII (Cont'd)

Summary of Hypervelocity Crater Depth Data

Section (2)   Copper Sphere Impinging Against Aluminum Plate at
Normal Incidence

Source	Impact Velocity km/sec	Apparent Depth Eglin or ARO cm	Apparent Depth NBS cm	Apparent Depth Average cm	Sphere Residue cm	Real Depth cm
Sphere Diameter 1/16 in.						
ARO-Inc.	0.772	0.229	0.113	0.171	-	0.171
ARO-Inc.	1.312	0.380	0.383	0.381	0.045	0.426
ARO-Inc.	1.912	0.500	0.503	0.502	0.032	0.534
ARO-Inc.	2.276	0.546	0.548	0.547	0.024	0.571
Eglin AFB	2.419	0.493	0.567	0.530	0.024	0.554
Eglin AFB	3.627	0.757	0.749	0.753	0.015	0.768
Eglin AFB	4.234	0.792	0.826	0.809	-	0.809
Eglin AFB	4.770	0.759	0.786	0.772	0.016	0.788
Eglin AFB	5.380	0.744	0.749	0.746	-	0.746
ARO-Inc.	5.687	0.833	0.866	0.850	-	0.850
ARO-Inc.	6.090	0.917	0.876	0.896	-	0.896
ARC-Inc.	6.436	0.917	0.908	0.912	-	0.912
Sphere Diameter 1/8 in.						
Eglin AFB	0.741	0.533	0.539	0.536	0.011	0.547
ARC-Inc.	1.278	0.833	0.828	0.831	0.098	0.929
ARC-Inc.	1.673	0.988	1.019	1.004	0.068	1.072
ARO-Inc.	2.133	1.097	1.172	1.135	0.058	1.193
ARC-Inc.	2.240	1.185	1.173	1.179	0.055	1.234
Eglin AFB	2.707	1.181	1.076	1.128	0.047	1.175
Eglin AFB	3.200	1.377	1.384	1.380	0.044	1.424
Eglin AFB	3.449	1.374	1.401	1.388	0.027	1.415
Eglin AFB	3.580	1.374	1.467	1.420	0.033	1.453
ARO-Inc.	3.604	1.476	1.481	1.478	0.018	1.496
ARO-Inc.	4.206	1.631	1.656	1.643	0.040	1.683
ARO-Inc.	5.340	1.897	1.865	1.881	-	1.881
Sphere Diameter 3/16 in.						
ARO-Inc.	2.690	1.966	1.979	1.972	-	1.972
ARC-Inc.	3.086	2.047	2.077	2.062	0.057	2.119
ARO-Inc.	3.496	2.258	2.273	2.266	-	2.266
ARO-Inc.	3.740	2.276	2.289	2.282	0.079	2.361

TABLE VII (Cont'd)

Summary of Hypervelocity Crater Depth Data

Section (3) Aluminum Sphere Impinging Against Aluminum Plate at Normal Incidence

Source	Impact Velocity km/sec	Apparent Depth Eglin or ARO cm	Apparent Depth NBS cm	Apparent Depth Average cm	Sphere Residue cm	Real Depth cm
- - - - - - - - - - - - - - Sphere Diameter 1/16 in. - - - - - - - - - - - - - - -
Eglin AFB	0.489	0.046	0.049	0.047	-	0.047
Eglin AFB	1.289	0.104	0.111	0.108	0.038	0.146
Eglin AFB	2.629	0.229	0.232	0.230	0.017	0.247
ARO-Inc.	3.200	0.245	0.255	0.250	-	0.250
Eglin AFB	3.216	0.284	0.269	0.276	0.013	0.289
ARO-Inc.	4.076	0.310	0.307	0.309	0.008	0.317
Eglin AFB	4.128	0.335	0.318	0.326	0.014	0.340
Eglin AFB	4.345	0.323	0.325	0.324	-	0.324
Eglin AFB	4.436	0.352	0.349	0.350	0.008	0.358
Eglin AFB	4.875	0.335	0.360	0.348	-	0.348
Eglin AFB	4.900	0.257	0.378	0.317	0.023	0.340
Eglin AFB	5.128	0.371	0.368	0.370	0.025	0.395
ARO-Inc.	5.322	0.355	0.357	0.356	0.011	0.367
		0.354	0.354	0.354	-	0.354
ARO-Inc.	6.654	0.392	0.402	0.397	0.029	0.426
ARO-Inc.	6.793	0.398	0.392	0.395	-	0.395
ARO-Inc.	6.924	0.373	0.384	0.378	-	0.378
ARO-Inc.	7.292	0.425	0.413	0.419	-	0.419
ARO-Inc.	7.507	0.462	0.414	0.438	-	0.438

TABLE VII (Cont'd)

Summary of Hypervelocity Crater Depth Data

Section (3) Aluminum Sphere Impinging Against Aluminum Plate at Normal Incidence

Source	Impact Velocity km/sec	Apparent Depth Eglin or ARO cm	Apparent Depth NBS cm	Apparent Depth Average cm	Sphere Residue cm	Real Depth cm
- - - - - - - - - - Sphere Diameter 1/8 in. - - - - - - - - - - - - - -						
Eglin AFB	1.498	0.302	0.288	0.295	0.050	0.345
ARO-Inc.	2.048	0.399	0.393	0.396	0.039	0.435
Eglin AFB	2.106	0.419	0.423	0.421	0.030	0.451
ARO-Inc.	2.254	0.445	0.429	0.437	0.032	0.469
ARO-Inc.	2.263	0.445	0.432	0.439	0.033	0.472
ARO-Inc.	2.317	0.408	0.387	0.397	0.037	0.434
ARO-Inc.	2.348	0.469	0.390	0.429	-	0.429
ARO-Inc.	2.548	0.570	0.555	0.562	0.012	0.574
Eglin AFB	3.315	0.630	0.629	0.630	0.014	0.644
Eglin AFB	3.987	0.625	0.638	0.632	0.020	0.652
Eglin AFB	4.026	0.625	0.639	0.632	0.028	0.660
ARO-Inc.	4.549	0.730	0.736	0.733	0.017	0.750
Eglin AFB	4.566	0.696	0.707	0.702	0.021	0.723
ARO-Inc.	4.820	0.678	0.657	0.667	0.016	0.683
Eglin AFB	5.060	0.594	0.736	0.665	-	0.665
ARO-Inc.	5.148	0.758	0.756	0.757	-	0.757
ARO-Inc.	5.289	0.789	0.793	0.791	-	0.791
ARO-Inc.	5.612	0.829	0.825	0.827	-	0.827
ARO-Inc.	5.694	0.790	0.786	0.788	0.026	0.814
ARO-Inc.	5.751	0.737	0.725	0.731	0.024	0.755
ARO-Inc.	5.880	0.828	0.800	0.814	0.019	0.833
ARO-Inc.	6.920	0.936	0.934	0.935	0.019	0.954

TABLE VII (Cont'd)

Summary of Hypervelocity Crater Depth Data

Section (3)   Aluminum Sphere Impinging Against Aluminum Plate at Normal Incidence

Source	Impact Velocity km/sec	Apparent Depth Eglin or ARO cm	Apparent Depth NBS cm	Apparent Depth Average cm	Sphere Residue cm	Real Depth cm

- - - - - - - - - - - -Sphere Diameter 3/16 in.- - - - - - - - - - - - -

Source	Impact Velocity km/sec	Apparent Depth Eglin or ARO cm	Apparent Depth NBS cm	Apparent Depth Average cm	Sphere Residue cm	Real Depth cm
ARO-Inc.	2.548	0.799	0.808	0.804	0.040	0.844
ARO-Inc.	2.977	0.895	0.917	0.906	0.025	0.931
ARO-Inc.	3.024	0.898	0.899	0.898	0.026	0.924
ARO-Inc.	3.049	0.905	0.914	0.909	0.027	0.936
ARO-Inc.	3.107	0.902	0.908	0.905	0.026	0.931
ARO-Inc.	3.131	0.926	0.934	0.930	0.026	0.956
ARO-Inc.	3.146	0.913	0.909	0.911	0.025	0.936
ARO-Inc.	3.447	0.951	0.947	0.949	0.022	0.971
ARO-Inc.	4.223	1.088	1.085	1.087	-	1.087
ARO-Inc.	4.727	1.194	1.178	1.186	0.020	1.206
ARO-Inc.	5.166	1.298	1.272	1.285	-	1.285
ARO-Inc.	5.404	1.296	1.280	1.288	-	1.288
ARO-Inc.	6.632	1.337	1.325	1.331	-	1.331
ARO-Inc.	6.884	1.363	1.353	1.358	-	1.358
ARO-Inc.	6.876	1.334	1.320	1.327	-	1.327
ARO-Inc.	6.925	1.392	1.377	1.384	-	1.384
ARO-Inc.	7.306	1.429	1.421	1.425	-	1.425

Section (4)   Aluminum Sphere Impinging Against Copper Plate at Normal Incidence

- - - - - - - - - - - -Sphere Diameter 1/16 in. - - - - - - - - - - - -

Source	Impact Velocity	Eglin or ARO	NBS	Average	Residue	Real Depth
Eglin AFB	1.408	0.033	0.034	0.034	0.045	0.079
Eglin AFB	1.417	0.030	0.031	0.030	0.032	0.062
ARO-Inc.	1.748	0.097	0.065	0.081	0.014	0.095
Eglin AFB	2.373	0.091	0.091	0.091	0.015	0.106
Eglin AFB	2.777	0.094	0.092	0.093	0.027	0.120
Eglin AFB	2.955	0.122	0.122	0.122	0.011	0.133
ARO-Inc.	3.134	0.124	0.109	0.116	0.014	0.130
Eglin AFB	3.318	0.140	0.145	0.142	0.011	0.153
ARO-Inc.	3.513	0.153	0.151	0.152	-	0.152
ARO-Inc.	3.603	0.163	0.166	0.164	-	0.164
Eglin AFB	4.525	0.188	0.162	0.175	0.003	0.178
Eglin AFB	4.566	0.157	0.167	0.162	0.001	0.163
ARO-Inc.	5.106	0.214	0.201	0.207	-	0.207
ARO-Inc.	6.020	0.237	0.240	0.238	0.004	0.242
ARO-Inc.	6.106	0.229	0.216	0.222	-	0.222
ARO-Inc.	6.539	0.240	0.248	0.244	0.005	0.249
ARO-Inc.	7.205	0.254	0.220	0.237	0.003	0.240

TABLE VII (Cont'd)

Summary of Hypervelocity Crater Depth Data

Section (4) Aluminum Sphere Impinging Against Aluminum Plate at Normal Incidence

Source	Impact Velocity km/sec	Apparent Depth Eglin or ARO cm	Apparent Depth NBS cm	Apparent Depth Average cm	Sphere Residue cm	Real Depth cm
--------- Sphere Diameter 1/8 in. ---------						
Eglin AFB	0.562	-	-	-	0.051	0.051
Eglin AFB	1.465	-	0.078	-	0.070	0.148
ARO-Inc.	1.833	0.149	0.149	0.149	0.045	0.194
Eglin AFB	2.160	0.196	0.204	0.200	0.034	0.234
ARO-Inc.	2.324	0.199	0.202	0.200	0.017	0.217
ARO-Inc.	2.990	0.268	0.259	0.264	0.034	0.298
Eglin AFB	3.828	0.325	0.318	0.322	0.008	0.330
Eglin AFB	3.912	0.340	0.337	0.338	0.003	0.341
ARO-Inc.	4.357	0.396	0.392	0.394	-	0.394
Eglin AFB	4.566	0.338	0.345	0.342	0.007	0.349
Eglin AFB	4.616	0.386	0.373	0.380	0.002	0.382
ARO-Inc.	4.710	0.376	0.370	0.373	0.003	0.376
Eglin AFB	5.201	0.335	0.334	0.334	0.002	0.336
ARO-Inc.	5.514	0.425	0.422	0.424	0.004	0.428
ARO-Inc.	6.141	0.461	0.452	0.456	0.003	0.459
ARO-Inc.	6.400	0.478	0.471	0.474	-	0.474
ARO-Inc.	6.944	0.525	0.509	0.517	-	0.517
--------- Sphere Diameter 3/16 in. ---------						
ARO-Inc.	2.697	0.374	0.399	0.386	0.043	0.429
ARO-Inc.	2.973	0.384	0.368	0.376	0.018	0.394
ARO-Inc.	3.729	0.503	0.500	0.502	0.004	0.506
ARO-Inc.	3.914	0.528	0.529	0.528	-	0.528
ARO-Inc.	4.396	0.641	0.644	0.642	0.004	0.646
ARO-Inc.	4.645	0.574	0.582	0.578	0.003	0.581
ARO-Inc.	4.969	0.591	0.586	0.589	0.005	0.594
ARO-Inc.	5.309	0.662	0.657	0.659	-	0.659
ARO-Inc.	5.328	0.634	0.630	0.632	-	0.632
ARO-Inc.	5.377	0.609	0.611	0.610	-	0.610
ARO-Inc.	6.022	0.693	0.693	0.693	0.002	0.695
ARO-Inc.	6.106	0.682	0.688	0.685	-	0.685
ARO-Inc.	6.262	0.613	0.606	0.609	0.002	0.611
ARO-Inc.	6.386	0.734	0.738	0.736	-	0.736
ARO-Inc.	6.563	0.722	0.720	0.721	-	0.721
ARO-Inc.	6.869	0.766	0.761	0.764	0.004	0.768
ARO-Inc.	6.896	0.784	0.787	0.785	0.002	0.787
ARO-Inc.	6.950	0.755	0.757	0.756	-	0.756

REFERENCES

1. Olive G. Engel, "Pits in Metals Caused by Collision with Liquid Drops and Soft Metal Spheres," NBS Journal of Research 62, 229 (1959).

2. Olive G. Engel, "Pits in Metals Caused by Collision with Liquid Drops and Rigid Steel Spheres", NBS Journal of Research 64A, 61 (1960).

3. Olive G. Engel, WADD-TR-60-475 Part II, "Crater Depth in Fluid Impacts," November 1962.

4. Jack H. Rupe, "Critical Impact Velocities of Water Droplets as a Problem in Injector-Spray Sampling," Progress Report No. 4-80, Jet Propulsion Laboratory, California Institute of Technology, Pasadena, California, September 1950.

5. Proceeding of Sixth Hypervelocity Impact Symposium, Cleveland, Ohio, April 30 - May 2 1963, to be published.

6. A. E. Olshaker and R. L. Bjork, "The Role of Melting and Vaporization in Hypervelocity Impact," Proceedings of Fifth Symposium on Hypervelocity Impact, Colorado School of Mines, Denver, Colorado, April 1962.

7. See Proceedings of the First Six Symposia on "Hypervelocity Impact, and, in Particular, Proceedings of the Third Symposium on "Hypervelocity Impact," Volume I, Armour Research Foundation, Chicago, Illinois, February 1959.

8. S. S. Rogers and L. Mandelkern, J. Phys. Chem. 61, 985 (1957).

9. C. D. Liles and E. H. Goodman, "Particle-Solid Impact Phenomena," Technical Documentary Report No. AEDC-TDR-62-202 November 1962.

10. Olive G. Engel, "Collisions of Liquid Drops with Liquids," NBS Technical Note No. 89, May 1961.

11. Olive G. Engel, "Symposium on Erosion and Cavitation," ASTM Special Technical Publication No. 307, 1961.

DOCUMENT CONTROL DATA - R&D

(Security classification of title, body of abstract and indexing annotation must be entered when the overall report is classified)

1. ORIGINATING ACTIVITY (Corporate author)	2a. REPORT SECURITY CLASSIFICATION
National Bureau of Standards Washington, D.C.	N/A
	2b. GROUP N/A

3. REPORT TITLE

COLLISIONS OF LIQUID DROPS WITH LIQUIDS
Part III. Impact Cratering In The Hypervelocity Range

4. DESCRIPTIVE NOTES *(Type of report and inclusive dates)*

WADD-TR-60-475, Summary Technical Report- June 1965

5. AUTHOR(S) *(Last name, first name, initial)*

Engel, Olive G.

6. REPORT DATE	7a. TOTAL NO. OF PAGES	7b. NO. OF REFS
June 1966	73	11

8a. CONTRACT OR GRANT NO. AF 33(657)-62-385	9a. ORIGINATOR'S REPORT NUMBER(S)
b. PROJECT NO. 7342	WADD-TR-60-475, Part III
c.	9b. OTHER REPORT NO(S) *(Any other numbers that may be assigned this report)*
d.	N/A

10. AVAILABILITY/LIMITATION NOTICES

Distribution Of This Document Is Unlimited

11. SUPPLEMENTARY NOTES	12. SPONSORING MILITARY ACTIVITY AFML (MANC) Wright-Patterson AFB, Ohio 45433

13. ABSTRACT

Results of analysis of information obtained from photographs of a hypervelocity impact against a transparent target and from hypervelocity craters produced in impacts that involved the four possible projectile-target combinations of high-purity copper and aluminum are discussed. An equation for hypervelocity crater depth is derived. Hypervelocity crater depth data for the four possible projectile-target combinations of high-purity copper and aluminum are presented in table form and used in graphs to test the theoretical equations.

14.		LINK A		LINK B		LINK C	
KEY WORDS		ROLE	WT	ROLE	WT	ROLE	WT

INSTRUCTIONS

1. **ORIGINATING ACTIVITY:** Enter the name and address of the contractor, subcontractor, grantee, Department of Defense activity or other organization *(corporate author)* issuing the report.

2a. **REPORT SECURITY CLASSIFICATION:** Enter the overall security classification of the report. Indicate whether "Restricted Data" is included. Marking is to be in accordance with appropriate security regulations.

2b. **GROUP:** Automatic downgrading is specified in DoD Directive 5200.10 and Armed Forces Industrial Manual. Enter the group number. Also, when applicable, show that optional markings have been used for Group 3 and Group 4 as authorized.

3. **REPORT TITLE:** Enter the complete report title in all capital letters. Titles in all cases should be unclassified. If a meaningful title cannot be selected without classification, show title classification in all capitals in parenthesis immediately following the title.

4. **DESCRIPTIVE NOTES:** If appropriate, enter the type of report, e.g., interim, progress, summary, annual, or final. Give the inclusive dates when a specific reporting period is covered.

5. **AUTHOR(S):** Enter the name(s) of author(s) as shown on or in the report. Enter last name, first name, middle initial. If military, show rank and branch of service. The name of the principal author is an absolute minimum requirement.

6. **REPORT DATE:** Enter the date of the report as day, month, year; or month, year. If more than one date appears on the report, use date of publication.

7a. **TOTAL NUMBER OF PAGES:** The total page count should follow normal pagination procedures, i.e., enter the number of pages containing information.

7b. **NUMBER OF REFERENCES:** Enter the total number of references cited in the report.

8a. **CONTRACT OR GRANT NUMBER:** If appropriate, enter the applicable number of the contract or grant under which the report was written.

8b, 8c, & 8d. **PROJECT NUMBER:** Enter the appropriate military department identification, such as project number, subproject number, system numbers, task number, etc.

9a. **ORIGINATOR'S REPORT NUMBER(S):** Enter the official report number by which the document will be identified and controlled by the originating activity. This number must be unique to this report.

9b. **OTHER REPORT NUMBER(S):** If the report has been assigned any other report numbers *(either by the originator or by the sponsor)*, also enter this number(s).

10. **AVAILABILITY/LIMITATION NOTICES:** Enter any limitations on further dissemination of the report, other than those imposed by security classification, using standard statements such as:

(1) "Qualified requesters may obtain copies of this report from DDC."

(2) "Foreign announcement and dissemination of this report by DDC is not authorized."

(3) "U. S. Government agencies may obtain copies of this report directly from DDC. Other qualified DDC users shall request through

_____."

(4) "U. S. military agencies may obtain copies of this report directly from DDC. Other qualified users shall request through

_____."

(5) "All distribution of this report is controlled. Qualified DDC users shall request through

_____."

If the report has been furnished to the Office of Technical Services, Department of Commerce, for sale to the public, indicate this fact and enter the price, if known.

11. **SUPPLEMENTARY NOTES:** Use for additional explanatory notes.

12. **SPONSORING MILITARY ACTIVITY:** Enter the name of the departmental project office or laboratory sponsoring *(paying for)* the research and development. Include address.

13. **ABSTRACT:** Enter an abstract giving a brief and factual summary of the document indicative of the report, even though it may also appear elsewhere in the body of the technical report. If additional space is required, a continuation sheet shall be attached.

It is highly desirable that the abstract of classified reports be unclassified. Each paragraph of the abstract shall end with an indication of the military security classification of the information in the paragraph, represented as *(TS), (S), (C),* or *(U)*.

There is no limitation on the length of the abstract. However, the suggested length is from 150 to 225 words.

14. **KEY WORDS:** Key words are technically meaningful terms or short phrases that characterize a report and may be used as index entries for cataloging the report. Key words must be selected so that no security classification is required. Identifiers, such as equipment model designation, trade name, military project code name, geographic location, may be used as key words but will be followed by an indication of technical context. The assignment of links, rules, and weights is optional.